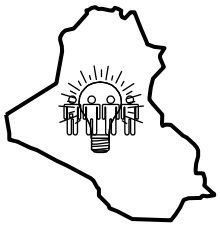

SPONSORED AND PUBLISHED BY
THE IRAQI SOCIETY FOR ALTERNATIVE AND RENEWABLE ENERGY SOURCES AND TECHNIQUES (I.S.A.R.E.S.T.)

EDITORIAL BOARD

ADVISORY BOARD

Storing Light in Optical Fibers Using Sound Waves

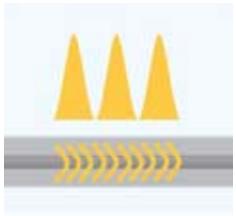

Written by
Zhaoming Zhu, Daniel Gauthier
Department of Physics, Duke University, Durham, NC, USA
Robert Boyd
The Institute of Optics, University of Rochester, Rochester, NY, USA

An optical pulse sequence can be stored in a hypersonic material excitation, then retrieved after an adjustable time interval using stimulated Brillouin scattering.

Increasing traffic on the Internet demands faster optical transmission networks. Future high-speed communication networks may rely largely on all-optical components that are intrinsically faster than their electronic counterparts. To achieve such networks, however, one needs to overcome a number of obstacles that exist at levels from devices to systems. For example, the lack of all-optical memory for storing optical data remains a bottleneck in modern optical information networks.[1] There has been substantial progress in addressing this problem using spatial-spectral holography in systems that operate at cryogenic temperatures[2] or stored light based on electromagnetically induced transparency, where optical information is impressed upon internal degrees of freedom of an ensemble of atoms or ions.[3] Both of these methods, however, are limited to operating at the resonance wavelength of the ions or atoms used. These limitations have recently been partially overcome using a dynamically controlled resonator in which a single optical pulse was stored for ~100ps.[4]

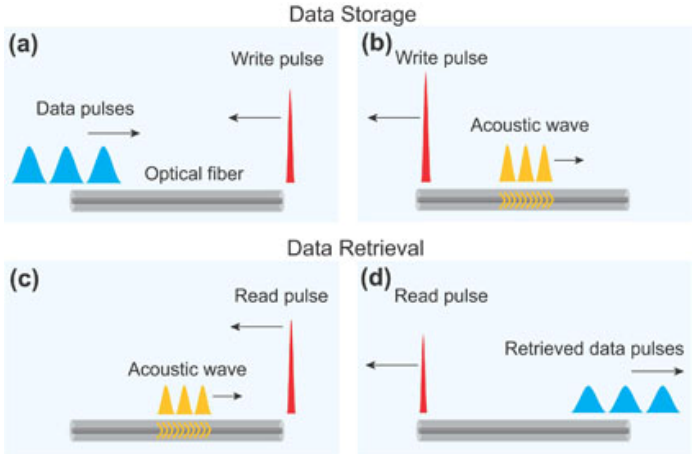

Fig. (1) Stimulated Brillouin scattering allows data storage in an optical fiber. In the storage process, (a) optical data pulses interact with a 'write' pulse . (b) The optical data pulses become depleted as the information shifts to an acoustic wave in the fiber. To retrieve the data, (c) a 'read' pulse depletes the acoustic wave, (d) generating a replica of the original data pulses.

We recently presented a different approach: a simple stored-light approach[5] in which optical pulse information is transferred onto a slowly moving hypersonic wave (~1/40,000 of the light speed) in an optical fiber and converted back at a later time through stimulated Brillouin scattering (SBS) as illustrated in Figure 1. In the storage process, optical data pulses (of carrier frequency ν_0) interact with a counterpropagating short intense 'write' pulse (of carrier frequency $\nu_0+\nu_B$, where ν_B is the Brillouin frequency shift of the fiber). The optical data pulses become depleted as energy is shifted to a hypersonic wave in the fiber. In the retrieval process, a short intense 'read' pulse at the same frequency as the 'write' pulse depletes the acoustic wave and releases the data back to the original optical frequency, thereby generating a replica of the incident data pulses. This stored-light approach has advantages such as room-temperature operation at any wavelength within the fiber transparency window, and the use of off-the-shelf components.

Our stored-light approach can obtain high storage and retrieval efficiency when four conditions are satisfied.[5] The first condition is that the 'area' of the write and read pulses must equal $\pi/2$, which determines the peak power requirement for these pulses. Another condition is that the write and read pulses must be shorter than the shortest-duration data pulse in order to achieve faithful storage and retrieval of data pulses. Third, the

storage time T_s (the time separation between the write and read pulses) must be less the acoustic lifetime τ_B, because the exponential decay of the acoustic wave reduces the readout efficiency until the data is eventually lost. Finally, the spatial extent of the data packet must be less than twice the length of the storage material.

In our recent experiment,[5] we used two 1.55μm tunable diode lasers to create the write, read, and data pulses and used a 5m-long highly-nonlinear fiber (with a ν_B~9.6GHz and τ_B~3.4ns) as the medium for storing light. We cascaded several erbium-doped fiber amplifiers to obtain 1.5ns-long write and read pulses with the required peak powers of ~100W. The system stored 2ns-long data pulses for up to 12ns with good readout efficiency, and demonstrated the potential of our approach for storing data packets that contain many pulses.

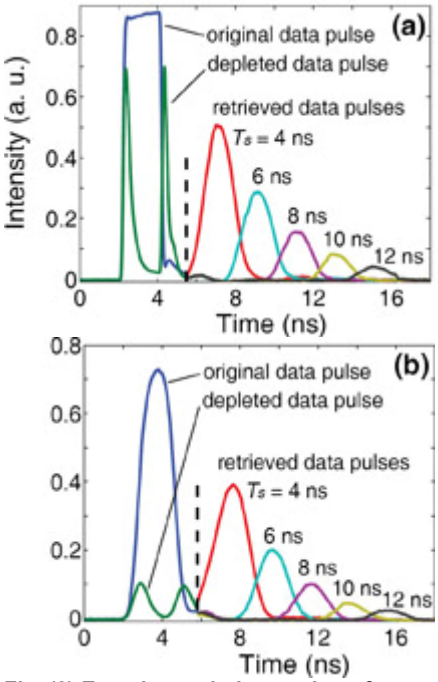

Fig. (2) Experimental observation of stored light. (a) Results for a 2ns rectangular-shaped data pulse. (b) Results for a 2ns smooth data pulse. The retrieved pulses are shown with a scale factor of two.[5]

Figure 2(a) shows results for storing and retrieving a single rectangular-shaped 2ns data pulse. (The incident data pulse is shown to the left of the dashed vertical line by the blue line.) About 66% of the incident pulse energy is depleted in the storage process, indicating a faithful transfer of optical pulse information onto the acoustic wave. The curves to the right of the dashed vertical line are the retrieved pulses for various T_s, which are scaled by a factor of two for clarity. The readout efficiency (defined as the ratio of the energy of the released pulse to that of the incident data pulse) is 25% for T_s = 4ns, and 1.8% for T_s = 12ns. As expected, the readout efficiency drops with increasing storage time due to the decay of the acoustic wave. We also stored and retrieved a smoothed-edge 2ns data pulse—Figure 2(b)—for which the energy storage efficiency increases to 86% and the readout efficiencies are improved slightly (~29% for T_s = 4ns, ~2% for T_s=12ns).

Figures 3(a) and 3(b) show our observations for the storage and retrieval of sequences of two and three data pulses, respectively. For clarity, we show only the input data pulses to the left of the dashed vertical line, and to the right we show the retrieved pulses scaled by a factor of five. The retrieved light replicates the input data stream with reasonable fidelity.

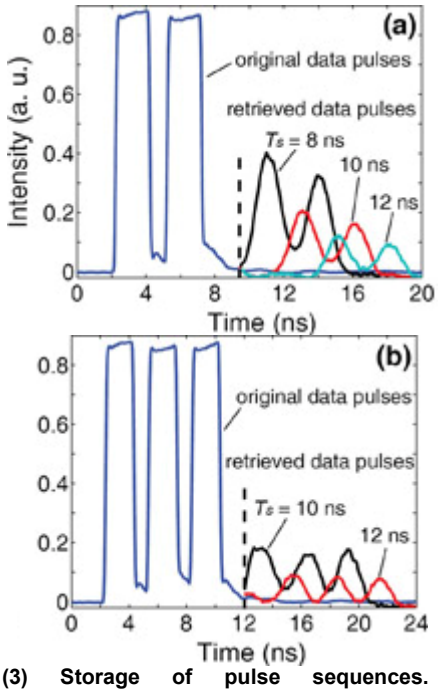

Fig. (3) Storage of pulse sequences. (a) Experimental results for two 2ns data pulses. (b) Experimental results for three 2ns data pulses. The retrieved pulses are shown with a scale factor of five.[5]

In summary, we demonstrated a simple approach for coherent light storage which allows us to store 2ns pulses for up to 12ns in an optical fiber with reasonable retrieval efficiencies. This stored-light technique can be improved by using fibers that exhibit longer acoustic lifetime (which will allow longer storage time and higher retrieval efficiency) and higher Brillouin sensitivity (which would reduce the peak power requirements of the write and read pulses). We anticipate that our method will be useful in all-optical memories and information processing such as correlation and convolution.

References

1. R. S. Tucker, P.-C. Ku, C. J. Chang-Hasnain, Slow-light optical buffers: capabilities and fundamental limitations, *J.Lightwave Technol.* 23, no. 12, pp. 40-46, 2005.
2. H. Lin, T. Wang, T. W. Mossberg, Demonstration of 8-Gbit / in.2, areal storage density based on swept-carrier frequency-selective optical memory, *Opt. Lett.* 20, no. 15, pp. 16-58, 1995.
3. C. Liu, Z. Dutton, C. H. Behroozi, L. V. Hau, Observation of coherent optical information storage in an atomic medium using halted light pulses, *Nature* 409, no. 6819, pp. 490, 2001.
4. Q. Xu, P. Dong, M. Lipson, Breaking the delay-bandwidth limit in a photonic structure, *Nature Phys* 3, no. 6, pp. 406, 2007.
5. Z. Zhu, D. J. Gauthier, R. W. Boyd, Stored light in an optical fiber via stimulated Brillouin scattering, *Science* 318, no. 5857, pp. 1748, 2007.

Organized by I.S.A.R.E.S.T.

INVITATION TO PARTICIPATE

WHAT IS ENERGY?

Energy is neither created nor destroyed. This is called the principle of Conservation of Energy. In other words, the amount of energy in the universe always remains the same. And when we use energy, like burning wood to generate light and heat, we don't use it up; we simply transform it from one form of potential energy (fuel) into other forms of kinetic energy (heat and light).

Almost all energy transformations involve the production of heat, which is considered the lowest form of energy, because it quickly dissipates into the surroundings and is normally unavailable for further use. So, although the total amount of energy remains the same, the amount of "useable" energy constantly decreases. However, don't worry too much about the decrease of useable energy; our Sun is scheduled to produce solar energy for many years to come, so taking this course will not be a waste of your time (or energy).

Energy is all around us. It heats our homes, powers our light bulbs and appliances, fuels our cars and provides for a variety of professional careers that deal with its many elements. It also comes in many forms such as heat, light, chemical, mechanical and electrical energy. And, according to physicists, energy can neither be created nor destroyed, only converted from one form to another. So why learn about energy? The answer is because energy, and the conversion of energy from one form to another, is fundamental to our modern living environment. By knowing the principles behind energy generation and conversion, you will come away with a knowledge base that can be applied to nearly every modern electrical, mechanical and chemical device that uses or produces power.

To introduce more about the alternative and renewable energy sources and techniques, I.S.A.R.E.S.T. invites you to attend the scientific lectures organized by I.S.A.R.E.S.T. You are requested to contact the secretary of the society and register your attendance. The lectures can be held earlier due to the registered requests.

To all they would like to submit seminars or scientific lectures during the third semester of the **I.S.A.R.E.S.T.** (July, August and September) in 2008, you are kindly requested to contact the secretary of the **I.S.A.R.E.S.T.** for date and presentation arrangements of the seminars or lectures. Please, do not hesitate to participate in our activities, this chance might be required by young scientists in our country, IRAQ, to develop and grow as well as introduce the professors and experts in field. You could find us on the post address, emails and mobile below:

Mailing Address:

P. O. Box 55259, Baghdad 12001, IRAQ

Emails:

irq_appl_phys@yahoo.com

editor_ijap@yahoo.co.uk

odayata2001@yahoo.com

Mobile:

00964-7901274190

Yulong Shen
George G. Malliaras

Materials Science and Engineering,
Cornell University, Ithaca
New York, U.S.A
yls60@cornell.edu

Charge Injection into Organic Semiconductors

In this work, the dependence of injection on the degree of doping of an organic semiconductor was studied. A model organic semiconductor, tetra-methyl triphenyl diamine doped polycarbonate (PC:TMTPD) was used for these experiments. By substituting TMTPD molecules with a TMTPD+SbF_6- salt, the degree of doping in the organic semiconductor was systematically varied. Changes in the electrical characteristics of devices with various electrodes were analyzed to yield the dependence of injection on the degree of doping. Along with the doping concentration, the temperature and distance between electrodes was also varied. This provided a better understanding of how doping, temperature and electrode spacing affect device performance.

Keywords: *Organic semiconductors, Charge injection, OLED's*
Received 4 January 2008, Revised 2 March 2008, Accepted 9 March 2008

1. Introduction

The observation of efficient electroluminescence in organic semiconductors a decade ago gave new momentum to the field of organic optoelectonics. Organic light emitting diodes (OLEDs) are currently under intensive development in both academia and industry for applications in flat panel displays [1]. The first commercial product, a car stereo display, was introduced in the market three years ago by Pioneer. Last year, Philips opened an OLED pilot plant, while Motorola recently announced that it will begin introducing OLED displays in cell phones as early as next year. Today, almost every major consumer electronics company and a lot of smaller start-up companies in the United States and overseas have experimental programs in OLED development.

This renewed interest in organic semiconductors due to OLEDs has had beneficial effects in other organic-based devices too. Organic thin film transistors have recently reached performance similar to that of amorphous silicon transistors [2], while organic solar cells are reaching energy conversion efficiencies exceeding 1%, a five orders of magnitude increase since the early 70s [3]. Many believe that these advances are signaling the beginning of the era of "plastic electronics", an era where inexpensive, organic-based electronic components will become available. IBM is currently running a TV commercial that shows a futuristic supermarket in which electronic tags placed on every item ensure completely automated checkout. Inexpensive electronic components will change the face of our world as we know it.

Essential for the operation of all organic optoelectronic devices is the process of charge injection (or extraction) from metal electrodes into the organic semiconductor. In OLEDs, the efficiency of charge injection is the single most important factor in determining the efficiency [4]. Efficient charge injection is also very important for good performance in organic thin film transistors [2]. Despite the importance of charge injection at the metal/organic interface, we know very little about the fundamentals of this process. This is mainly because of two reasons. First, knowledge from inorganic semiconductors cannot be directly translated to the case of organic materials due to the different nature of charge transport in the latter. Second, in the majority of device studies, the process of charge injection cannot be easily separated from the process of charge transport. In addition to the technological importance, understanding the process of charge injection is a fundamental problem that is too beautiful to ignore.

2. Measuring Charge Injection

As with traditional semiconductors, a metal/organic contact can be Ohmic or current-limiting. In the former case the contact supplies adequate current to satisfy the demands of the organic layer, while in the latter it creates a bottleneck in the current flow. A figure-of-merit is the injection efficiency η

$$\eta = \frac{J_{INJ}}{J_{SCL}} \qquad (1)$$

where J_{INJ} is the density of the net current injected by the contact and J_{SCL} is the space charge limited current density.

For the case of trap-free materials (which we know how to synthesize thanks to advances in

electrophotography [5]), J_{SCL} is given by the Mott-Gurney law [6]:

$$J_{SCL} = \frac{9}{8}\frac{\varepsilon\varepsilon_0\mu V^2}{L^3} \quad (2)$$

where ε_0 is its dielectric constant, μ is the charge carrier mobility, assumed here to be field independent, V is the applied voltage and L is the thickness. By definition, η=1 for an Ohmic contact and η<1 for a limiting contact.

The injection efficiency can be measured with a technique developed by Abkowitz et al [7]. A variation of this technique, which is appropriate for monopolar materials (where only one of the carriers is mobile), is shown in Fig. (1). The polarity of the applied bias in the figure is appropriate for a hole-transport material. First, the mobility of the carriers in the organic is measured with a time-of-flight experiment [5] and the space charge limited current is calculated according to Eq. (2). Second, the polarity of the applied bias is reversed and the current injected from the contact under test is directly measured.

For the time-of-flight experiment, a non-injecting ("blocking") contact ensures a negligible dark current. A strongly absorbed pulse of light excites a thin sheet of carriers inside the organic, just underneath the blocking contact. The transient photocurrent is measured as this sheet of carriers' drifts towards the opposite electrode. The photocurrent drops to zero as soon as the carriers arrive at the opposite electrode. The mobility is calculated from the time it takes the carriers to transit the sample.

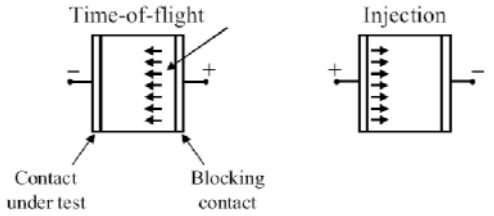

Fig. (1) Layout of the experiment for the measurement of the injection efficiency. The polarity of the bias indicated here is for a hole-transport organic semiconductor

The injection efficiency at the metal/organic interface is a complex function of many parameters. The interface energetics play an important role, as carriers might have to overcome an energy barrier to be injected into the organic. The composition and the morphology at the interface play an important role too, as they can have an effect on the interface energetics. Systematic studies that carefully isolate and measure the influence of each parameter are very important for understanding the injection process. Generally, organic materials form well-defined contacts: A variety of studies find that the energy barrier at the metal/organic interface scales with the difference of the appropriate energy levels of the metal and the organic [8-12], indicating the absence of energy level pinning. This is reflected in the process of charge injection: Recent measurements of the hole injection efficiency in an organic semiconductor show that η increases with the work function of the injecting electrode [7].

In addition to forming well defined interfaces, organic semiconductors offer unique degrees of freedom that can be used to probe the fundamentals of the injection process. Consider, for example, tetraphenylene diamine doped polycarbonate (PC:TPD), which is one of the most well studied organic semiconductors. The mobile species is holes, which move by hopping among TPD molecules. By varying the relative concentration of TPD into PC, one can change the hole mobility by several orders of magnitude without disturbing the interface energetics. We have used this degree of freedom to explore the dependence of injection on mobility. As an injecting electrode we used Indium Tin Oxide (ITO), which is commonly used in OLEDs.

Experimental results are shown in Fig. (2). The injection efficiency was measured at a constant electric field in six samples with a TPD concentration ranging from 30 to 100%. The mobility is varied for three orders of magnitude, yet the injection efficiency remains constant at about 3%. Therefore, ITO forms a current limiting contact with PC:TPD, regardless of the mobility.

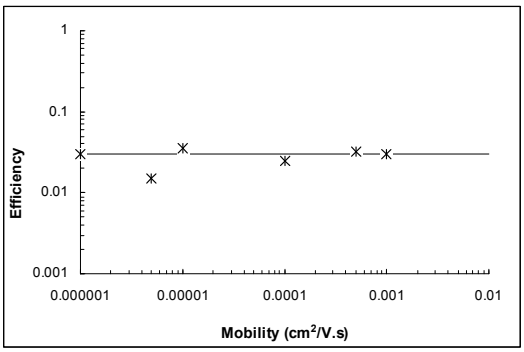

Fig. (2) Injection efficiency of the ITO/PC:TPD contact as a function of mobility in PC:TPD. Each data point corresponds to a different sample, with a different concentration of TPD. The solid line is a guide to the eye

The above results may appear surprising at first. One might expect that the number of carriers that "boil-over" from the contact into the organic per unit time is solely determined by the energy barrier at the interface and it is therefore fixed. If the bulk is slow (low mobility), these carriers will be enough to sustain a space charge limited current. As the bulk gets faster, the injection efficiency should drop. The fact that η

is independent of mobility means that the injected current (J_{INJ}) depends on the transport properties of the organic. An explanation for this behavior is given below.

3. Theory and Discussion

Extending existing injection models developed for crystalline materials to treat injection at the metal organic interface is not straightforward. This is because charge transport in organic semiconductors takes place not by free propagation in extended states but rather by hopping between localized states. The recent interest in metal/organic interfaces has prompted the development of a variety of new models, which are reviewed in reference1. Here we outline the features of a simple model that predicts a mobility dependent injection.

Since mobilities are low in organic materials, it is to be expected that surface recombination of injected carriers will play a very important role in determining the current at the interface [13]. The net injected current density J_{INJ} will be equal to:

$$J_{INJ} = J_{MO} - J_{OM} \quad (3)$$

where J_{MO} is the current density injected from the metal to the organic and J_{OM} is the backflow (recombination) current density.

Scott and Malliaras [14] developed a simple model based on the premise that surface recombination at the metal/organic is a field-enhanced diffusion process, entirely analogous to Langevin bimolecular recombination in amorphous semiconductors. This allows for a straightforward calculation of the surface recombination current density, J_{OM}, which, for zero field, is found to be equal to:

$$J_{OM} = \frac{16\pi\varepsilon\varepsilon_0\mu n_0 (KT)^2}{e^2} \quad (4)$$

where μ is the mobility and n_0 is the charge density at the interface. Using detailed balance (J_{MO}=J_{OM} at zero field), J_{MO} is equal to:

$$J_{MO} = \frac{16\pi\varepsilon\varepsilon_0\mu N_0}{e^2}\exp\left(-\frac{\phi_B}{KT}\right) \quad (5)$$

where N_0 is the density of states in the organic and ϕ_B is the Schottky energy barrier. Note that the above equation can be rewritten in terms of an effective Richardson constant, which, for typical parameters for the organic, is four orders of magnitude smaller than the free electron value [14].

The above equations are for the zero field case. Taking the field dependence of surface recombination and barrier lowering into account, we can calculate the net injected current density:

$$J_{INJ} = 4\psi^2\mu e N_0 E\exp\left(-\frac{\phi_B}{KT}\right)\exp\left(f^{\frac{1}{2}}\right) \quad (6)$$

where ψ is a slowly varying function of electric field and the exponential in the square root of electric field, $f = e^3E/4\pi\varepsilon\varepsilon_0(KT)^2$, represents the usual Schottky barrier lowering effect. Here the mobility is assumed to be independent of the electric field. The three currents are plotted in Fig. (3) for ϕ_B=0.55eV. It can be seen that J_{MO} and J_{OM} are of comparable magnitude, indicating that surface recombination does indeed play a major role in determining the net injected current.

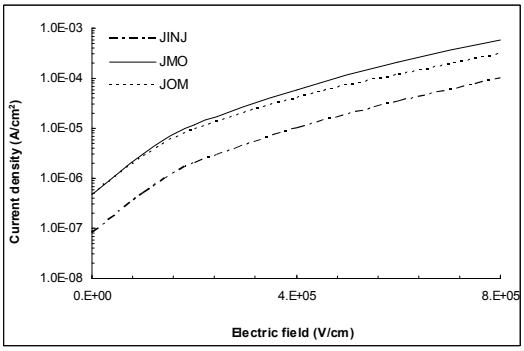

Fig. (3) Electric field dependence of the currents at the metal/organic for μ=5x10^{-5}cm^2/V.sec and ϕ_B=0.55eV

The model gives a rather good prediction for the electric field dependence of η. In Fig. (4), experimental data for the sample with 60% TPD in PC are compared to calculated values for barrier heights of 0.50 and 0.55eV. The model reproduces the dip and the subsequent increase of η with electric field. Moreover, the predicted barrier height is within the expected range [15]. The actual electric field dependence of η is a bit steeper, probably due to the electric field dependence of the mobility in PC:TPD.

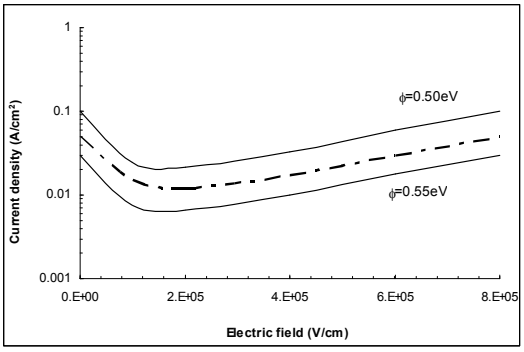

Fig. (4) Electric field dependence of the injection efficiency of the ITO/PC:TPD contact for a sample containing 60% TPD in PC. The solid lines are the predictions of the theory for ϕ_B=0.50eV and 0.55eV

4. Conclusions

The field of organic optoelectronics is currently enjoying a golden era. Organic light

emitting diodes are on the threshold of commercialization, while other organic-based devices are being developed at an incredible pace. All these devices rely on efficient charge injection from metal electrodes. At this point, however, our fundamental understanding of the charge injection process is very limited. Understanding this process will allow us to optimize metal/organic interfaces and increase device performance.

Organic semiconductors have undergone several years of development for applications in electrophotography and are now available with tailored, well-defined charge transport properties. An important lesson we learned from all these years of development is that organic semiconductors are "model systems" for the study of a wide variety of charge transport phenomena. We can and we should capitalize on this knowledge to explore the properties of metal/organic interfaces. There is a lot of beautiful science to be done!

References

[1] Scott, J.C.; Malliaras, G.G. in **"Semiconducting Polymers: Chemistry, Physics and Engineering"**; van Hutten, P. F.; Hadziioannou, G., Eds.; WILEY-VCH (New York), 1999.
[2] Klauk, H.; Jackson, T.N. *Solid State Technology* 2000, *43*, 63.
[3] Schon, J.H.; Kloc, C.; Bucher, E.; Batlogg, B. *Nature* 2000, *403*, 408.
[4] Malliaras, G.G.; Scott, J.C. *J. Appl. Phys.* 1998, *83*, 5399.
[5] Borsenberger, P.M.; Weiss, D.S. **"Organic Photoreceptors for Imaging Systems"**; Marcel Dekker (New York), 1998.
[6] Lambert, M.A.; Mark, P. **"Current Injection in Solids"**; Academic Press (New York), 1970.
[7] Abkowitz, M.; Facci, J.S.; Rehm, J. *J. Appl. Phys.* 1998, *83*, 2670.
[8] Campbell, I.H.; Hagler, T.W.; Smith, D.L.; Ferraris, J.P. *Phys. Rev. Lett.* 1996, *76*, 1900.
[9] Seki, K.; Ito, E.; Ishii, H. *Synth. Met.* 1997, *91*, 137.
[10] Malliaras, G.G.; Salem, J.R.; Brock, P.J.; Scott, J. C. *J. Appl. Phys.* 1998, *84*, 1583.
[11] Schlaf, R.; Merritt, C.D.; Crisafulli, L.A.; Kafafi, Z.H. *J. Appl. Phys.* 1999, *86*, 5678.
[12] Ishii, H.; Sugiyama, K.; Ito, E.; Seki, K. *Adv. Mater.* 1999, *11*, 605.
[13] Emtage, P.R.; O'Dwyer, J.J. *Phys. Rev. Lett.* 1996, *16*, 356.
[14] Scott, J.C.; Malliaras, G.G. *Chem. Phys. Lett.* 1999, *299*, 115.
[15] Shen, Y.; Klein, M.W.; Jacobs, D.B.; Scott, J.C.; Malliaras, G.G., submitted for publication.

This article was reviewed at Department of Physics, College of Science, University of Hadhramout – Seyoun, YEMEN and School of Applied Sciences, University of Technology, Baghdad, IRAQ

Sponsored and Organized by

Institute of Physics (IOP)

THE SIXTH INTERNATIONAL CONFERENCE ON GRAVITATION AND COSMOLOGY (ICGC-2007)
17–21 December 2007, Inter-University Centre for Astronomy and Astrophysics (IUCAA), Ganeshkhind, Pune University Campus, Pune 411 007, India
http://meghnad.iucaa.ernet.in/~icgc07/index.html

15TH INTERNATIONAL SYMPOSIUM ON ELECTRON MOLECULE COLLISIONS AND SWARMS
2–4 August 2007, University of Reading, Berkshire, UK
http://web.am.qub.ac.uk/posmol07/

ELECTROSTATICS 2007
25–29 March 2007, St Catherine's College, Oxford

PHYSICS-BASED MATHEMATICAL MODELS OF LOW-DIMENSIONAL SEMICONDUCTOR NANOSTRUCTURES: ANALYSIS AND COMPUTATION
18–23 November 2007, Banff International Research Station, Banff, Canada
http://www.birs.ca

THE THIRD INTERNATIONAL CONFERENCE OF THE AFRICAN MATERIALS RESEARCH SOCIETY
7–10 December 2005, Marrakech, Morocco

MONTE CARLO TECHNIQUES IN RADIOTHERAPY DELIVERY AND VERIFICATION: THIRD MCGILL INTERNATIONAL WORKSHOP
29 May to 1 June 2007, McGill University, Montréal, Canada
http://www.medphys.mcgill.ca/~mcworkshop2007/Welcome.html

FIRST INTERNATIONAL CONGRESS OF THE INTERNATIONAL ASSOCIATION OF INVERSE PROBLEMS (IPIA)
25–29 June 2007, University of British Columbia Campus, Vancouver, Canada
http://www.pims.math.ca/science/2007/07aip/

SECOND SCHOOL ON COSMIC RAYS AND ASTROPHYSICS
Puebla, Mexico, 30 August – 8 September 2006

IV CONGRESS OF THE VENEZUELAN PHYSICAL SOCIETY
December 2007, Merida, Venezuela

RADIATION DAMAGE IN BIOMOLECULAR SYSTEMS
19–22 June 2007, The Royal College of Surgeons, Dublin, Ireland

SYMMETRY AND STRUCTURAL PROPERTIES OF CONDENSED MATTER
5–12 September 2007, Myczkowce, Poland

DISSOCIATIVE RECOMBINATION 2007
18–23 July 2007, Ameland, The Netherlands
http://www.ru.nl/molphys/dr2007/proceedings

GR18/7TH AMALDI MEETING
8–14 July 2007, Sydney, Australia
http://www.grg18.com

H-MODE PHYSICS AND TRANSPORT BARRIERS
26–28 September 2007, Tsukuba, Japan
http://www-jt60.naka.jaea.go.jp/h-mode-tm-11

ELECTRON MICROSCOPY AND ANALYSIS GROUP CONFERENCE 2007 (EMAG 2007)
3–7 September 2007, Glasgow Caledonian University & The University of Glasgow, UK
http://www.iop.org/Conferences/Forthcoming_Institute_Conferences/event_8375.html

17TH INTERNATIONAL VACUUM CONGRESS (IVC-17), 13TH INTERNATIONAL CONFERENCE ON SURFACE SCIENCES (ICSS-13)AND INTERNATIONAL CONFERENCE ON NANOSCIENCE AND TECHNOLOGY (ICN+T2007)
2–6 July 2007, Stockholm, Sweden
http://www.congrex.com/ivc17icss13/

13TH INTERNATIONAL CONFERENCE ON LIQUID AND AMORPHOUS METALS (LAM 13)
8–14 July 2007, Ekaterinburg, Russia

V INTERNATIONAL SYMPOSIUM ON QUANTUM THEORY AND SYMMETRIES
22–28 July 2007, Valladolid, Spain

15TH INTERNATIONAL COUETTE TAYLOR WORKSHOP
9–12 July 2007, Le Havre, France

COMPUTING IN HIGH ENERGY AND NUCLEAR PHYSICS (CHEP)
2–7 September 2007, Victoria, British Columbia, Canada

http://www.chep2007.com/

2007 EUROPHYSICS CONFERENCE ON HIGH ENERGY PHYSICS
19–25 July 2007, Manchester, UK
http://www.hep.man.ac.uk/HEP2007/

INTERNATIONAL NATHIAGALI SUMMER COLLEGE ON PHYSICS AND CONTEMPORARY NEEDS
25 June – 7 July 2007, Nathiagali, Pakistan
http://www.ncp.edu.pk/INSC/index.htm

TOPICS IN ASTROPARTICLE AND UNDERGROUND PHYSICS (TAUP 2007)
11–15 September 2007, Sendai, Japan
http://www.awa.tohoku.ac.jp/taup2007/

INTERNATIONAL CONFERENCE ON NON-COMMUTATIVE GEOMETRY AND PHYSICS
23–27 April 2007, Laboratoire de Physique Theorique, Universite Paris XI, France

THE FIFTH INTERNATIONAL CONFERENCE ON INERTIAL FUSION SCIENCE AND APPLICATIONS (IFSA2007)
9–14 September 2007, Kobe, Japan

PLASMA THEORY, WAVE KINETICS, AND NONLINEAR DYNAMICS
5–7 October 2007, University of California, Berkeley, USA
http://web.mac.com/aecharman/iWeb/KaufmanFest2007

395TH WE-HERAEUS SEMINAR: TIME-DEPENDENT PHENOMENA IN QUANTUM MECHANICS
12–16 September 2007, Blaubeuren, Germany
http://www.quantumdynamics.de

JOINT 21ST AIRAPT AND 45TH EHPRG INTERNATIONAL CONFERENCE ON HIGH PRESSURE SCIENCE AND TECHNOLOGY
17–21 September 2007, Catania, Italy

INTERNATIONAL SYMPOSIUM ON ADVANCED NANODEVICES AND NANOTECHNOLOGY
2–7 December 2007, Waikoloa, Hawaii, USA
http://www.fulton.asu.edu/~nano/ISANN.htm

THE SECOND INTERNATIONAL SYMPOSIUM ON ATOMIC TECHNOLOGY
1–2 October 2007, Hyogo, Japan

FIFTEENTH INTERNATIONAL SUMMER SCHOOL ON VACUUM, ELECTRON, AND ION TECHNOLOGIES (VEIT 2007)
17–21 September 2007, Bulgaria
http://www.veit.8k.com

HELIOSEISMOLOGY, ASTEROSEISMOLOGY AND MHD CONNECTIONS
20–24 August 2007, Gottingen, Germany

INTERNATIONAL SYMPOSIUM ON VACUUM SCIENCE & TECHNOLOGY
28–30 November 2007, Mubai, India

5TH INTERNATIONAL CONFERENCE ON MAGNETIC AND SUPERCONDUCTING MATERIALS (MSM07)
25–30 September 2007, Khorezm Mamun Academy of Sciences, Khiva, Uzbekistan

INTERNATIONAL SYMPOSIUM ON LATTICE EFFECTS IN CUPRATE HIGH TEMPERATURE SUPERCONDUCTORS
31 October – 3 November 2007, Tsukuba, Japan

4TH WORLD CONGRESS ON BIOMIMETICS, ARTIFICIAL MUSCLES AND NANO-BIO
6–9 November 2007, Cartagena, Spain

2007 INTERNATIONAL SYMPOSIUM ON NONLINEAR DYNAMICS
27–30 October 2007, Shanghai, China
http://www.2007isnd.com

8TH EUROPEAN CONFERENCE ON APPLIED SUPERCONDUCTIVITY
16–20 September 2007, Brussels, Belgium
http://www.eucas2007.org/

7TH WORKSHOP ON INFORMATION OPTICS
1–5June 2008, Annecy, France
http://wio2008.univ-st-etienne.fr/

INTERNATIONAL WORKSHOP 60 YEARS OF CASIMIR EFFECT
23–27 June 2008, International Center of Condensed Matter Physics, Brasilia, DF, Brazil
http://www.iccmp.web.br.com/en/evento_19.php

AB INITIO SIMULATION OF CRYSTALLINE SOLIDS: HISTORY AND PROSPECTS
8–9 September 2008, Torino, Italy

SCIENTIFIC DISCOVERY THROUGH ADVANCED COMPUTING 2008 (SCIDAC 2008)
13–17 July 2008, Fairmont Olympic Hotel, Seattle, Washington, USA
http://hpcrd.lbl.gov/SciDAC08/SciDAC.html

2ND NATIONAL CONFERENCE ON NANOTECHNOLOGY "NANO 2008"
25–28June 2008, Jagiellonian University, Krakow, Poland
http://confer.uj.edu.pl/nano2008/index.php?□=en

A Mathematical Model to Describe the Densification Process During the Sintering of Ceramic Compacts

Ahmad K. Ahmad [1]
Fadhil A. Rasen [2]
Sadeem A. Fadhil [1]

[1] *Department of Physics, College of Science, Al-Nahrain University, Baghdad, Iraq*
abnkamal@yahoo.com
[2] *Department of Physics, College of Science, Babylon University, Babylon, Iraq*

A mathematical model describing the densification process during viscous sintering process of a ceramic material contains solid inclusions is developed (modified) from the Scherer model which describes the rate of densification during sintering for a free solid inclusions material. The modification is performed by assuming that the unit cell is composed from three types of constituent; the solid inclusions phase, the porous phase and the viscous phase. The solid inclusions phase is assumed to block the propagation of the viscous phase through the cylinders that assumed to be found through the body of the compact. The modified model is used to study the effect of several factors on densification during sintering process and used in predicting the effective viscosity of the viscous phase that formed during sintering.

Keywords: *Ceramic compacts, Sintering, Densification process*
Received: 20 January 2007, Revised: 18 May 2008, Accepted: 20 May 2008

1. Introduction

The starting of the theory of viscous sintering began in 1945 when Frenkel [1] assumed that the energy dissipated in viscous flow is equal to the energy gained by the decrease in surface area during densification. Using this assumption, he obtained expressions for the rate of growth of a neck between glass spheres and for the rate of linear shrinkage of a compact of glass spheres. Mackenzie and Shuttleworth in 1949 [2] calculated the rate of densification of a viscous body containing closed spherical pores. They developed a model for the shrinkage of spherical bubbles in a viscous matrix. The simplicity of the geometry enabled them to write exact expressions for the energy dissipation and change in surface area during sintering. it most naturally applies to the last stages of densification, when the relative density is larger than 90% and the body contains only isolated closed pores. Scherer in 1977 [3] proposed a model which describes the rate at which a cubic array of cylinders densifies by viscous flow driven by surface energy reduction, the surface area change can be expressed exactly, but the assumed flow pattern was approximated. Scherer in 1987 [4] used two models of heterogeneous systems to approximate the viscous sintering in a material contains rigid inclusions. These models are the composite sphere model and the self consistent model. In the composite sphere model the compact is represented by a composite sphere with the core representing the solid inclusion. In the self-consistent model, the sintering material is regarded as being surrounded by a composite matrix with slower densification rate. The result differs only in that the shear modulus of the matrix is replaced by the shear modulus of the composite in the self-consistent calculation.

Eugene A. Olevsky and Charles W. Bert in 1997 [5] considered viscous sintering of a porous ball with various initial distributions of porosity versus radius. They elaborated the numerical algorithms based on the differential quadrature method (DQM) and an arbitrary Eulerian-Lagrangian version of the finite element method (FEM). Aldo R. Boccaccinia and Eugene A. Olevsky in 1999 [6] investigated The effect of rigid, (non-densifying) inclusions on the densification kinetics and shrinkage anisotropy during the sintering of composite glass powder compacts The experimental study was conducted on barium magnesium aluminosilicate (BMAS) glass composites containing Al_2O_3-platelets as a rigid inclusion phase. Andrey Maximenko and Eugene Olevsky in 2005 [7] modeled the pressure-assisted sintering of agglomerated powders by the grain boundary and the surface diffusion transport. They estimated the kinetics of sintering during consolidation by a direct numerical analysis of the matter redistribution by diffusion around a single neck between identical

spherical particles. Their calculations showed that, despite low initial density and low initial viscosity of a loose powder around agglomerates, isostatic pressing cannot provide a complete equalization of local densities in an agglomerated powder. In all considered cases, agglomerates have reached final density faster than elements with looser packing. In the present work Scherer geometrical model [3] is modified to make it take the effect of solid inclusions into consideration.

2. The Model

The geometrical model put by Scherer [3] is as shown in Fig. (1a) consists of a cubic array formed by intersecting cylinders. Each three cylinders intersect at a node. The cylinders represented the strings of oxide particles; the cylinder radius corresponded to the average particle radius in the Silica preform. A "unit cell" of the assumed structure is presented in Fig. (1b); when those cells are stacked, the structure shown in Fig. (1a) is obtained.

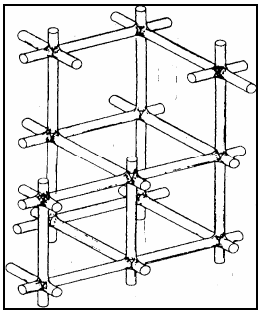

(a)

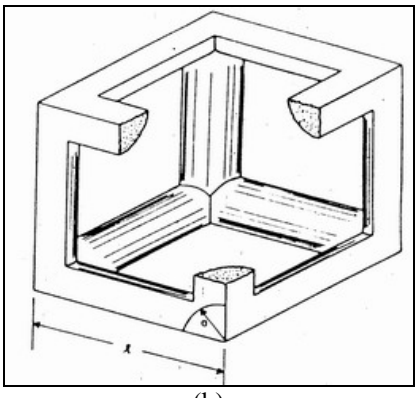

(b)

Fig. (1) Geometry of the Scherer model a) cylindrical array, b) Unit cell of the Scherer model, which is equivalent to the unit cell of the matrix structure in the present model [3]

The volume of the solid phase, V_S, in the cubic cell is determined by the equation [3]:

$$V_S = 3\pi a^2 l - 8\sqrt{2}a^3 \qquad (1)$$

where (***a***) is the cylinder radius and (***l***) is the side length of the unit cell. The last equation didn't consider the foundation of any solid inclusions, so in the case of the mixture of clays which consist from materials that will be discussed later, which contain relatively high ratio of rigid inclusions (that have the effect of retarding densification) the previous equation must be modified. The densification process in the composite will be simulated by manipulating the densification process in the matrix of the composite. We will assume that the solid inclusions are represented in the unit cell by a ratio equal their ratio in the compact, so if we suppose (λ) represents the ratio of the solid inclusions side length to the viscous phase side length in the compact, then (λ) can be defined as:

$$\lambda = \frac{l_{in}}{l_{vis}} = \left(\frac{V_{in}}{V_{vis}}\right)^{1/3} \qquad (2a)$$

where (V_{in} and l_{in}) are the theoretical volume and side length of solid inclusions in the compact, (V_{vis} and l_{vis}) are the theoretical volume and side length of viscous phase in the compact. Here the compact is assumed to have a cubic shape and the length of each constituent in the compact is assumed to equal the cubic root of its corresponding volume. The solid inclusions are assumed to be arranged in the unit cell in away, which reduces the side length of the unit cell (and as a result reduces the cylinder length) that the viscous phase can propagate through to achieve the densification. If the length of the unit cell that the viscous phase can propagate through is (l*), which will be called as the effective side length of the composite unit cell that equal the side length of the matrix, and if the side length of the composite unit cell is (l), which will be called as the compacted length, then at the end of the sintering process for the full densification the ratio of (l*) to (l) will equal the ratio of the viscous phase length (l_{vis}) to the summation of the solid inclusions length and the viscous phase length as in the equation

$$\frac{l^*}{l} = \frac{l_{vis}}{l_{vis} + l_{in}} \qquad (2b)$$

Substituting Eq. (2a) after rearranging in the right side of the last equation gives:

$$l^* = \frac{l}{1+\lambda} \qquad (2c)$$

The considered assumption will be as follows; the solid inclusions retard densification by decreasing the length of the cylinder, which the viscous phase can propagate through it. Therefore, the viscous phase is propagated through (l^*) not through (l), because the solid inclusions prevent the propagation of the viscous phase in the places where the solid inclusions are found. So each (l) in Scherer model will be replaced by (l^*), so Eq. (1) will be as:

$$V_S = 3\pi a^2 l^* - 8\sqrt{2}a^3 \qquad (3)$$

When there is no inclusions in the compact (i.e. λ=0) Eq. (3) will equal Eq. (1). As in Fig. (1b) the density, ρ, of the matrix cell is given by:

$$\rho = \frac{\rho_S V_S}{l^{*3}} \quad (4)$$

where ρ_s is the theoretical density of the solid phase. Combining Equations (3) and (4), we find that the relative density, ρ/ρ_s, is a function only of (a/l) and (λ), as the following equations declares:

$$\frac{\rho}{\rho_s} = 3\pi\left(\frac{a^2}{l^{*2}} - \frac{ca^3}{l^{*3}}\right) = 3\pi\frac{a^2}{l^{*2}}\left(1 - \frac{ca}{l^*}\right)$$

$$\frac{\rho}{\rho_s} = \frac{3\pi a^2(1+\lambda)^2}{l^2}\left(1 - \frac{ca(1+\lambda)}{l}\right) = \quad (5)$$

$$3\pi x^2(1+\lambda)^2\left(1 - cx(1+\lambda)\right)$$

where $c = 8\sqrt{2}/3\pi$, $x=a/l$. Fig. (2) shows the effect of the ratio (λ) on the relation between the relative density and the ratio (x) using Eq. (5).

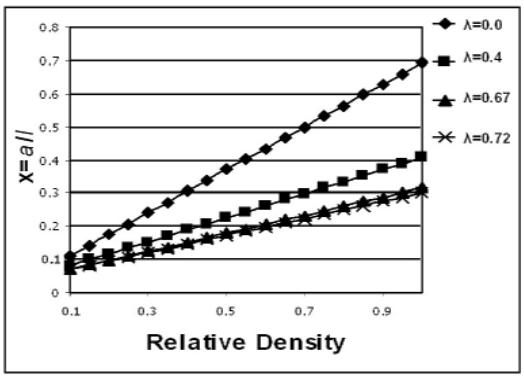

Fig. (2) *x* versus relative density, λ=0, 0.4, 0.67 and 0.72

Scherer [3] related the pore diameter (d), which may be obtained from Hg penetration porosimetry, to ($\boldsymbol{l}$) by equating the cross-sectional area of the pore with the area of the opening in the side of the cell. Replacing (l) with (l^*) this approach leads to:

$$\pi d^2/4 \approx (l^* - 2a)^2 \quad (6)$$

Scherer with these assumptions calculated the values of (a/l) for several preforms for which both particle size and porosimetry data were available. In the present case, this method can be applied for a given (λ) to find (a), but it will be more accurate if the Stereological ways is used with an image of scanning electron microscope to find (a) as will be seen later. Scherer [3] assumed that a cell consisting of twelve-quarter cylinders (or three full cylinders); replacing (l) by (l^*), and when the volume of the solid phase is apportioned among the three cylinders in the unit cell,

$$V_S = 3V_C \quad (7)$$

where V_C is the effective volume of one cylinder, and is given by

$$V_C = \pi a^2\left[l^* - (8\sqrt{2}/3\pi)a\right] \quad (8)$$

The quantity in brackets in Eq. (8) is the effective length of the cylinder. As the length of the cylinder decreases, the surface area of the cell decreases, as a result providing the driving force for the densification.

3. The Rate of Densification

To calculate the rate of densification the procedure used in reference [3] is followed and by replacing each (l) by (l^*) this gives:

$$\frac{dx}{dt} = \frac{\gamma}{2\eta}\frac{1}{l} \quad (9a)$$

where

$$x = \frac{a}{l} \quad (9b)$$

Recognizing that (V_s) is constant which means that the mass of solid matter is constant within the unit cell at any time so we can have:

$$l(t) = \frac{l_\circ(\rho_\circ/\rho_s)^{1/3}}{(1+\lambda)\left(\frac{3\pi x^2}{(1+\lambda)} - 8\sqrt{2}x^3\right)^{1/3}} \quad (10)$$

Substituting Eq. (10) into Eq. (9a) gives:

$$dx = \frac{\gamma}{2\eta}\frac{\left(\frac{3\pi x^2}{(1+\lambda)} - 8\sqrt{2}x^3\right)^{1/3}(1+\lambda)}{l_\circ(\rho_\circ/\rho_s)^{1/3}}dt \quad (11)$$

Rearranging the last equation in away that each side becomes a function of one variable and integrating on (t) in the interval from (t_o) to (t) on the (t) side of the equation, which corresponding to the interval from (x_o=0) to (x) on the (x), side of the equation gives:

$$K(t-t_\circ) = \int_0^x \frac{2dx}{(1+\lambda)\left(\frac{3\pi}{(1+\lambda)x} - 8\sqrt{2}\right)^{1/3}x} \quad (12)$$

where (K) is the proportionality constant between the reduced time (Kt) and the practical time (t_p)is given by:

$$K = \frac{\gamma}{\eta l_\circ}\left(\frac{\rho_s}{\rho_\circ}\right)^{1/3} \quad (13)$$

where t_o is the fictitious time at which (x=0). Eq. (12) determines (x) as a function of time; since for a certain value of (λ), ρ/ρ_s is a function only of x (t), so the density of the cell is determined as a function of time. The indefinite integral is readily evaluated with the substitution

$$y_x^3 = \frac{3\pi}{(1+\lambda)x} - 8\sqrt{2} \quad (14)$$

to give

$$K(t-t_\circ) = -\frac{2}{\alpha}(1+\lambda)^{-1}\left(\frac{1}{2}\ln\frac{\alpha^2 - \alpha y_x + y_x^2}{(\alpha+y_x)^2} + \right.$$

$$\left.\sqrt{3}\tan^{-1}\frac{2y_x - \alpha}{\alpha\sqrt{3}}\right) + K_o \quad (15a)$$

where $\alpha = (8\sqrt{2})^{1/3}$, ($K_o$) is a constant that corresponds to the value of (Kt) at $t=t_o$. From Eq. (13) and Eq. (15a), it is obvious that the viscosity is directly proportional with the factor (1+λ); in other word, the viscosity is increasing with increasing the solid inclusions. Scherer equation corresponding to Eq. (15a) was from reference [3] as

$$K(t-t_\circ) = -\frac{2}{\alpha}\left(\frac{1}{2}\ln\frac{\alpha^2-\alpha y_x+{y_x}^2}{(\alpha+y_x)^2} + \sqrt{3}\tan^{-1}\frac{2y_x-\alpha}{\alpha\sqrt{3}}\right)+K_o \qquad (15b)$$

and K_o has the same definition. According to the last equation, the relative density, ρ/ρ_s, can be plotted versus ($K(t)$) as done in reference [3]. The experimental data can be fitted to the theoretical curve by plotting the reduced times versus the experimentally determined times. Then the reduced times can be found from the plotted figure in the case of $\lambda=0$, or for general case from solving Eq. (15a) and Eq. (5) for x, and for known values of the relative density and λ. The slope of the straight line formed by plotting Kt as a function of experimental times of sintering equals (K). When Eq. (15) is applied to the experimental results for the sintering of mixtures of clays, after determining the value of (K) for each sample, it has been found that it is inapplicable. This is due to the assumption that at the beginning of the sintering process the value of (x) (which is given by the ratio (a/l)) is equal zero. This assumption may be applicable on the case of silica gel (as an example) or other materials stated in reference [8], but it is inapplicable on the materials of our present work, due to the solid inclusions and the anisotropy in the structure that found in the body of the compact. Therefore, the interval of the integration on (x) will be assumed to start at (x_o) following reference [9] with a difference, that (x_o) is not equal zero here. Applying this to the integration of Eq. (12) by starting the integration from (x_o) to (x), yield the following equation:

$$K(t-t_o) = -\frac{2}{\alpha}(1+\lambda)^{-1}\left[\left(\frac{1}{2}\ln\frac{\alpha^2-\alpha y_x+{y_x}^2}{(\alpha+y_x)^2} + \sqrt{3}\tan^{-1}\frac{2y_x-\alpha}{\alpha\sqrt{3}}\right) - \left(\frac{1}{2}\ln\frac{\alpha^2-\alpha y_{xo}+{y_{xo}}^2}{(\alpha+y_{xo})^2} + \sqrt{3}\tan^{-1}\frac{2y_{xo}-\alpha}{\alpha\sqrt{3}}\right)\right] \qquad (16a)$$

and the integration of Eq. (15b) will be:

$$K(t-t_o) = -\frac{2}{\alpha}\left[\left(\frac{1}{2}\ln\frac{\alpha^2-\alpha y_x+{y_x}^2}{(\alpha+y_x)^2} + \sqrt{3}\tan^{-1}\frac{2y_x-\alpha}{\alpha\sqrt{3}}\right) - \left(\frac{1}{2}\ln\frac{\alpha^2-\alpha y_{xo}+{y_{xo}}^2}{(\alpha+y_{xo})^2} + \sqrt{3}\tan^{-1}\frac{2y_{xo}-\alpha}{\alpha\sqrt{3}}\right)\right] \qquad (16b)$$

where

$$y_{xo}^3 = (3\pi/x_o) - 8\sqrt{2} \qquad (17)$$

and $x_0=a_0/l_0$, which is found from the initial relative density by numerically solving equation (5) for x, and the same procedure is applicable for any relative density at any time of the sintering process. Eq. (16) is more applicable and gives a good approximation to the density values, as will be seen later.

Scherer noted that the window in the side of the cubic cell closes when

$$a=l^*/2=l/(2(1+\lambda)) \qquad (18a)$$

where the side of the cell in Scherer model was equal (l), but in the present assumptions it is equal (l^*). So when ($\boldsymbol{a/l^*}$) =0.5, the neighboring cylinders touch and the cell contains a closed pore; the relative density at that instant according to Scherer and to the present model according to Eq. (5) is:

$$\frac{\rho}{\rho_s} = \left(\frac{3\pi}{4}\right) - \sqrt{2} = 0.942 \qquad (18b)$$

Scherer model and the present model are no longer applied for relative densities larger than that given by Eq. (5) because the structure cannot be described as an array of cylinders in these ranges of relative densities [3]. To limit the maximum value of (x) (x_{max}) corresponding to the relative density given by Eq. (18b) for the modified Scherer model, Eq. (18a) and Eq. (9b) gives the following equation:

$$\frac{a}{l^*} = \frac{a(1+\lambda)}{l} = x(1+\lambda) \qquad (19a)$$

So when (a/l^*) =0.5, then the maximum value of x (x_{max}) will be given by the following equation:

$$x_{\max} = \frac{0.5}{(1+\lambda)} \qquad (19b)$$

In the present materials (λ) usually has a value around (0.7), so from Eq. (19b), the highest value of (x) at which this model is still applicable is about 0.294 when ($\lambda=0.7$). For relative densities greater than 0.942, Scherer suggested using the analysis of Mackenzie and Shuttleworth [2] for viscous sintering of a body containing closed pores. Mackenzie and Shuttleworth plotted ρ/ρ_s versus the reduced time in the form:

$$\frac{\gamma n^{1/3}}{\eta}\left(t - t_o\right) = \frac{2}{3}\left(\frac{3}{4\pi}\right)^{1/3} \cdot \int_0^{\rho} \frac{d\rho_{rd}}{\left(1-\rho_{rd}\right)^{2/3}\rho_{rd}^{1/3}} \qquad (20a)$$

where (n) is the number of closed pores per unit volume of solid phase. ρ_{rd} is the relative density. Scherer supposed when x=0.5, the body consists of closed pores with $n=1/V_S$, or

$$n^{1/3} = \frac{1}{l_\circ}\left(\frac{\rho_s}{\rho_\circ}\right)^{1/3} \qquad (20b)$$

Using the same arguments used in finding Eq. (16a) it will be assumed that the integration in Eq. (20a) begins from initial value ρ_{rdo} and following reference [2] the assumption will be as:

$$z^3 = (1-\rho_{rd})/\rho_{rd} \qquad (20c)$$

by integration, the following formula will be given:

$$\frac{\gamma n^{1/3}}{\eta}\left(t - t_o\right) = \left[\frac{1}{2}\ln\frac{1+z^3}{(1+z)^3}\right] - \left[\sqrt{3}\tan^{-1}\frac{2z-1}{\sqrt{3}}\right] - \left[\frac{1}{2}\ln\frac{1+z_o^{\,3}}{(1+z_o)^3}\right] + \left[\sqrt{3}\tan^{-1}\frac{2z_o-1}{\sqrt{3}}\right] \qquad (21a)$$

where $z_o^3 = (1-\rho_{rdo})/\rho_{rdo}$

For the present model from Eq. (4) by comparison with Eq. (20b), the following equation will be concluded:

$$n^{1/3} = \frac{1}{l_\circ^*}\left(\frac{\rho_s}{\rho_\circ}\right)^{1/3} \qquad (21b)$$

Substituting Eq. (21b) into Eq. (21a), the left hand side becomes

$$\left(\frac{\gamma}{\eta l_\circ^*}\right)\left(\frac{\rho_s}{\rho_\circ}\right)^{1/3}\left(t - t_\circ\right) \qquad (21c)$$

Eq. (21c) differs from that in Scherer model by a factor $(1+\lambda)$ in the numerator. Thus to give the same time scale used in Eq. (16a), the equation of Mackenzie-Shuttleworth must be divided by a factor equal $(1+\lambda)$, or the final modified Mackenzie-Shuttleworth equation will be:

$$\frac{\gamma}{\eta l_\circ}\left(\frac{\rho_s}{\rho_\circ}\right)^{1/3}\left(t - t_o\right) = \left(1+\lambda\right)^{-1}\left[\left[\frac{1}{2}\ln\frac{1+z^3}{(1+z)^3}\right] - \left[\sqrt{3}\tan^{-1}\frac{2z-1}{\sqrt{3}}\right]\right] \qquad (22)$$

Once (K) has been determined by fitting the experimental results to the theoretical curve, then the measured values of $\boldsymbol{\rho_0}$ and $\boldsymbol{l_0}$ can be used to obtain the quantity (γ/η). If γ is assumed to equal 270erg/cm^2 then η can be found by substituting this value in Eq. (13) in addition to K value from fitting process. The fitting process is applied to two sample groups that are prepared by Rasen [10] and named M21 and M22. Group M21 is a mixture of compositional weight percentage of 60% kaolin raw material powder, 30% of ninivite raw material and 10% weight of α-Al_2O_3, Group M22 is a mixture of compositional weight percentage of 70% kaolin raw material mixed with 30% of ninivite raw material, the chemical composition of the raw materials of these groups is found in reference [11]. From fitting process and assuming γ equal to 270 erg/cm^2 which is the same value of γ of the silica (the major material that compose these two groups) the following figures (3 & 4) is obtained for the values of the viscosity coefficient as a function of sintering process for groups M21 & M22 respectively.

For comparison, figurers (5) and (6) show the values of effective viscosities versus sintering temperature for samples of groups M21 and M22 respectively as predicted by the Scherer model.

Scherer [4] put two models that describes the densification process during the sintering of materials that are sintered by viscous sintering but contain solid inclusions that have the effect to retard densification, these models are the Composite Sphere model (CS) and the Self Consistent model (S-C), the composite sphere model used to describe either the matrix densification (CS matrix) or the composite densification (CS composite), here the relations used by Scherer [4] will be applied for comparison with the results predicted from the present model. The basic relations used by (CS) models and the self consistent model (S-C) are found in reference [4] and the way to relate these relations to the practical data and the procedure to apply these relations is found in reference [11].

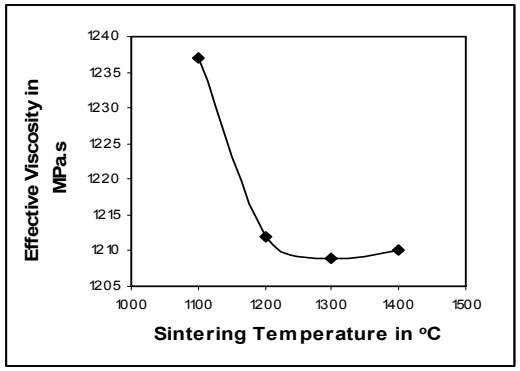

Fig. (3) Viscosity versus sintering temperature of samples of group M21 (λ=0.723) as predicted by the Modified Scherer Model

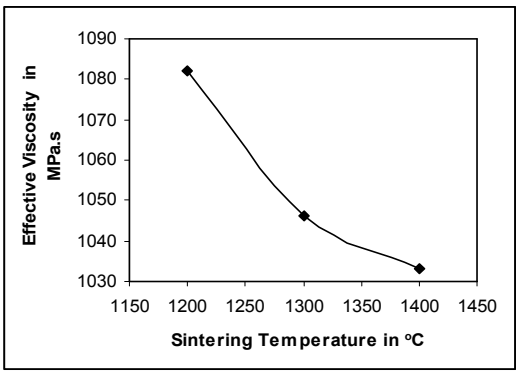

Fig. (4) Viscosity versus sintering temperature of samples of group M22 (λ=0.669) as predicted by the Modified Scherer Model

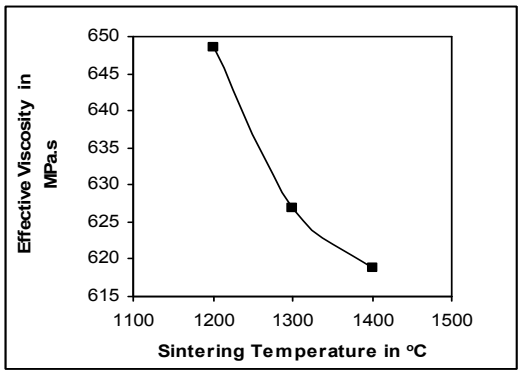

Fig. (6) Viscosity versus sintering temperature of samples of group M22 as predicted by the Scherer Model

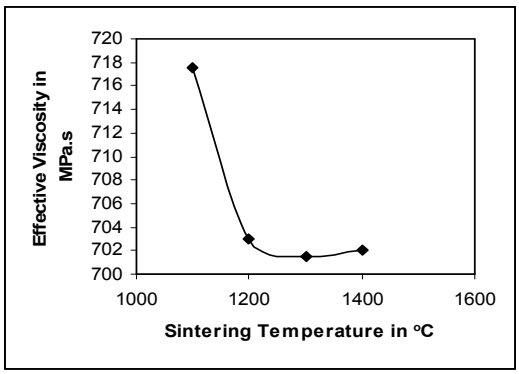

Fig. (5) Viscosity versus sintering temperature of samples of group M21as predicted by the Scherer Model

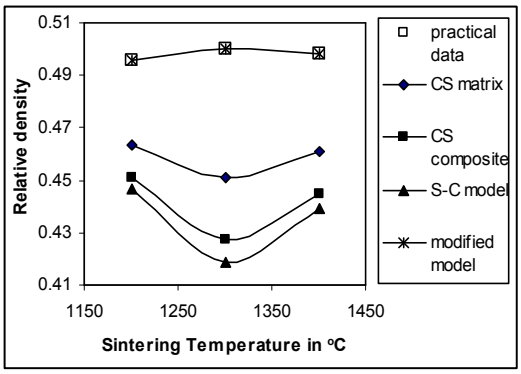

Fig. (7) Relative density from various heterogeneous models versus sintering temperature for samples of group M21 fired for two hours

4. Effect of Sintering Temperature on Density after Firing

By preparing samples which have the same composition and fired in different temperatures and after making fitting process to find (K) for each sample then the effect of firing temperature on densification process can be found in the curves in Fig. (7), which shows the predictions from the present model using Eq. (19a) in addition to the predictions from other models; like the composite sphere model (which describes the matrix densification (CS composite), and that which describes the composite densification (CS composite) and the self-consistent model (S-C).

5. Effect of Sintering Time on the Relative Density

By preparing samples of the same composition and by firing all samples at the same firing temperature but each sample is fired at a time duration differs from the result is in Fig. (8) for different values of the ratio (λ). In addition to compare the predictions of the effect of sintering time on densification process of the present model with the predictions from other models a simple program is made and the results are in Fig. (9).

6. Discussion

In this work the Scherer model for viscous sintering of open pore systems for materials such as glass or silica gel, which did not contain solid inclusions in a considerable amount is modified and applied to some heterogeneous multiphase systems that known to be sintered by viscous sintering and contains a considerable (non negligible) amount of solid inclusions such as some of the silicate systems (ex: kaolin) [12]. A unit cell is assumed as Scherer did, the cylinders penetrate the cell as in Fig. (1b), and the solid inclusions are supposed to be placed at the center of the cylinders. The solid inclusions are assumed to decrease the length side that the viscous phase can propagate through it and achieve densification. Each unit cell will contain a volume ratio from inclusions equal to the volume ratio in the compact.

According to these assumptions the formulas derived by Scherer [3,10] are modified and used to study the densification process during sintering for some of the Iraqi clays and to simulate the effect of several parameters on it. The first studied parameter is the effect of sintering temperature on the densification process. Here, also two models of heterogeneous systems (that also modified by Scherer) have

been applied to compare their results with the results from the modified model, and to study the applicability of each model. The models are the composite sphere model (which used to study the matrix densification (CS matrix) and the composite densification (CS composite)), and the self consistent (S-C) model.

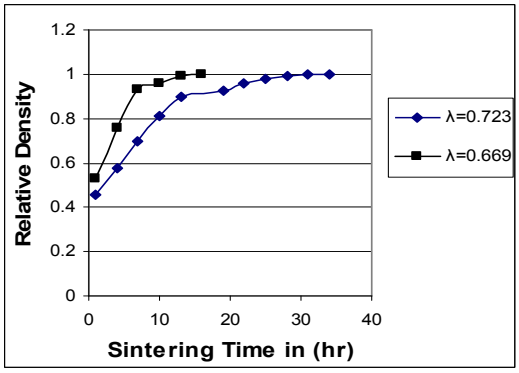

Fig. (8) Relative density versus sintering time for sample M21 (λ=0.723) and sample M22 (λ=0.669)

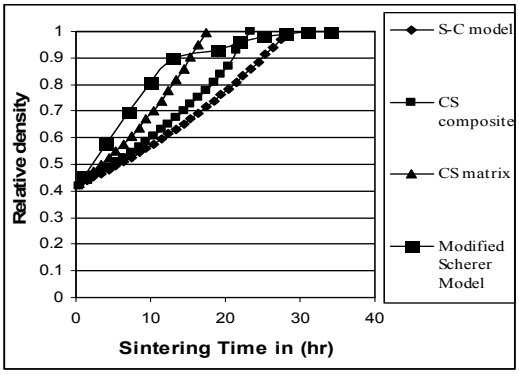

Fig. (9) Relative density versus sintering time for sample from group M21 (λ=0.723) sintered at temperature equal 1200°C found using various heterogeneous models as indicated in the list

From Fig. (3) it is obvious that for samples of group M21 the effective viscosity drops fast initially until a value of sintering temperature slightly above 1200°C where the curve stop decreasing and become a semi plateau curve. The semi plateau end is as a result of crystallization process. This indicates that the crystallization process largely affect the viscosity of the viscous phase in the compact as the predictions of reference [13].

From Fig. (4), for samples of group M22 it has been noted that the curve of the effective viscosity continues decreasing with temperature increasing, and no semi plateau end is found. This indicates that the crystallization process in samples of group M22 is less than that for M21. Also it has been noted that the magnitudes of the viscosity coefficient of samples of group M21 is higher than that for M22.This may be due to the higher ratio of solid inclusions (λ) in M21 especially from alumina, because high amounts reduce the mobility of liquid glassy phase, because of induced structural forms in the liquid phase [14]. This could induce crystallization in M21 and makes the values of viscosity for M21 higher than that for M22.

From figures (3) and (5) and figures (4) and (6) it is clear that the viscosity values predicted by the modified Scherer model equal about (1+λ) the viscosity values predicted by Scherer model. So the modified Scherer model predicts a higher effect for the solid inclusions in increasing the values of the effective viscosity of the viscous phase formed during the sintering process, unfortunately, there are no practical measurements of the effective viscosity for the simulated samples, so which value is correct this will be a proposal for the future work to prove it practically.

From Fig. (7), it is obvious that the results from the present modified model offer best applicability to the practical results. This may be due to the approximation for the value of interface energy, which is assumed to have the same value as that for silica, on the base that the silica represents the major material in the composite. The interface energy is applied in the case of the composite sphere and the self consistent models, while in applying the modified Scherer model there is no need to interface energy because the constant of proportionality between the reduced time and the practical time (K) is used directly to find the relative density, and this is an advantage point from the present model. Generally the composite sphere model is better applied to the densification than the self consistent model; this is due to the enormous liberties with the geometry of the material combination of the self consistent model [15].

Fig. (8) shows the densification process for samples of groups M22 and M21; for the values of x larger than x_{max} the modified Mackenzie-Shuttleworth model is used. The figure shows obviously the effect of solid inclusions on the values of the relative density versus sintering time. While M22 reaches a relative density equal 0.8 at firing time equal about five hours, sample M21 reaches the same relative density at firing time more than ten hours as the modified Scherer model predicts. So the solid inclusions strongly affect the densification process in viscous sintering and their effect on sample M21 was increasing the value of viscosity, and as a result retards densification.

Fig. (9) shows the predicted densification process for sample of group M21 with the modified Scherer model, the composite sphere model considering matrix and composite densification and the self consistent model. All the last three models predict an exponential

relation between the relative density and time, just the modified Scherer model predicted a semi logarithmic relation; unfortunately no detailed data is available for the densification process to limit which model is better applied, but the practical data from reference [6] which was for barium-magnesium aluminosilicate (BMAS) glass composites containing Al_2O_3-platelets as a rigid inclusion phase predicted a similar curve for the relative density versus time of sintering, also reference [16] predicted the same curve for porcelain. As it is obvious from Fig. (9), the modified Scherer model predicts that the densification is relatively fast at the initial stages of the sintering process, but at the last stages the densification rate becomes relatively slow. This happened because the densification rate is retarded due to full densification when the relative density approaches unity [13]. This part is predicted by the Mackenzie-Shuttleworth model, when the pores become closed pores and the rate of densification decreases.

7. Conclusion

The main concluded points can be summarized as follows:

1. The most limiting factor in the sintering of ceramic compacts that corresponded with the formation of viscous liquid is the magnitude of the effective viscosity of this liquid.
2. The solid inclusions have a strong effect in retarding the densification process, by increasing the value of the effective viscosity of the viscous liquid that is formed during sintering, which as a result decreases the rate of densification process.
3. The materials that can be regarded (or manipulated) as solid inclusions are the materials that didn't participate (or melted) in the viscous phase, and this is affected not only by the type of additive but also by the quantity of these additives, while a relatively little quantity of the materials (like alumina) reduces the viscosity of the viscous phase, a high quantity increases the viscosity and retards densification and act as solid inclusions as we saw in sample of group M21.

References

[1] J. Frenkel, *J. Phys* (USSR), 9 (1945) 385-91.

[2] 2. J. K. Mackenzie and R. Shuttleworth, *Proc. Phys. Soc.* (London), 62(12-B) (1949) 833-52.

[3] G. W. Scherer, *J. Am. Ceram. Soc.*, 60 (1977) 236-39.

[4] G.W. Scherer, *J. Am. Ceram. Soc.*, 70 (1987) 719-25.

[5] E. A. Olevsky and C. W. Bert, "Evolution of Porosity Distribution for One-Dimensional Problem of Viscous Sintering", *Commun. Numer. Methods in Eng.*, 13 (1997) 355-72.

[6] Aldo R. Boccaccinia and Eugene A. Olevsky, *J. Mater. Process. Technol.*, 96 (1999) 92-101.

[7] 7. Andrey Maximenko and Eugene Olevsky, *Int. J. Solids and Structures*, 42 (2005) 503-15.

[8] G. W. Scherer and D. L. Bachman, *J. Am. Ceram. Soc.*, 60 (1977) 239-43.

[9] G.W. Scherer, *J. Am. Ceram. Soc.*, 74 (1991) 1523-31.

[10] F. A. Rasen, "The Use of Iraqi Siliceous Rocks as Electrical Insulators in Industry", Ph.D. thesis in physics, Al-Nahrain University, Iraq (1998).

[11] S. A. Fadhil, "Mathematical Manipulation to Study the Changes of Porous Structure with the Formation Conditions of Porous Materials", M.Sc. thesis in Physics, Al-Nahrain University, Iraq (2005).

[12] F. H. Norton, Ch.15, **"Effect of Heat on Clay and Other Minerals"**, pp. 236-57 in **"Fine Ceramic: Technology and Applications"**, Robert E. Krieger Publishing Co. (Florida) (1987).

[13] P. C. Panda and W. M. Mobley and R. Raj, *J. Am. Ceram. Soc.*, 72 (1989) 2361-64.

[14] R. W. Grimshaw, Ch.11, **"Chemical Changes in Ceramic Materials"**, pp. 698-772 in **"The Chemistry and Physics of Clays and Allied Ceramic Materials"**, Ernest Benn Ltd. (London) (1971).

[15] R. M. Christensen, Ch.2, **"Effective Moduli: Spherical Inclusions"**, pp. 31-72 in **"Mechanics of Composite Materials"**, John Wiley & Sons (Toronto) (1979).

[16] W. D. Kingery, H. K. Bowen and D. R. Uhlmann, Ch.10, **"Grain Growth, Sintering, and Vitrification"**, pp. 448-515 in **"Introduction to Ceramics"**, John Wiley & Sons (Toronto) (1976).

This article was reviewed at Institute for Research and Nuclear Energy, IPEN CNEN/SP, BRAZIL, Department of Materials Science, Glass and Ceramics, University of Erlangen-Nuernberg, GERMANY, and School of Applied Sciences, University of Technology, Baghdad, IRAQ

Recent Developments

Biomaterials for Bone Tissue Engineering

Written by
Walid K. Hamoudi
School of Applied Sciences, University of Technology, Baghdad, IRAQ

Bone is a dynamic and highly vascularized tissue that continues to remodel throughout the lifetime of an individual. It plays an integral role in locomotion, ensures the skeleton has adequate load-bearing capacity, and acts as a protective casing for the delicate internal organs of the body. In addition, bone is intimately involved in homeostasis through its storage of Ca and P ions and by regulating the concentration of key electrolytes in the blood. More than 206 different bones make up the skeleton, ranging from the long bones found in our limbs, short bones in the wrist and ankle, and flat bones in the skull, to irregular bones such as the vertebrae.

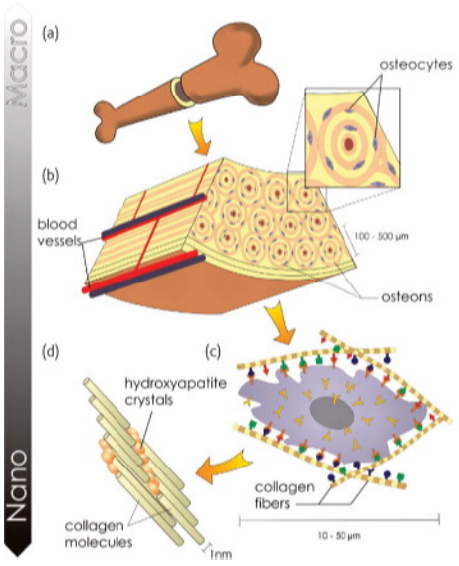

Materials that enhance bone regeneration have a wealth of potential clinical applications from the treatment of nonunion fractures to spinal fusion. The use of porous material scaffolds from bioceramic and polymer components to support bone cell and tissue growth is a longstanding area of interest. In younger people the majority of fractures heal well without the need for major intervention. However, large bone defects lack the template for regeneration and require surgical intervention. Transplanting bone from the patient has the best clinical outcome as it integrates reliably with host bone however; its use is severely hampered by its short supply. Scientists have shifted their interest from bio-inert toward 'bioactive' materials that integrate with biological molecules or cells and regenerate tissues. Materials should support bone growth and encourage the in-growth of surrounding bone and capable of integrating into surrounding bone. Bone substitute materials consist of bioactive ceramics, bioactive glasses, biological or synthetic polymers, and composites of these.

Bioactive glasses (Ca- and possibly P-containing silica glasses), for example, when immersed in biological fluid, can rapidly produce a bioactive hydroxyl-carbonated apatite layer that can bond to biological tissue. The brittle nature of bioactive inorganic materials means that their fracture toughness cannot match that of bone and on their own are not good for load-bearing applications. Biological polymers, such as collagen and hyaluronic acid, are interesting candidates for tissue engineering however, concern exists over immunogenicity, the potential risk of disease transmission, and weak mechanical properties. Synthetic polymers such as polyfumarates, polylactic acid, polyglycolic acid and polycaprolactone offer a versatile alternative. They are processable to produce a range of three-dimensional scaffolds with different porosities and surface characteristics. Inorganic-organic composites aiming to 'mimic' the composite nature of real bone combine the toughness of a polymer phase with the compressive strength of an inorganic one to generate bioactive materials with improved mechanical properties and degradation profiles.

For bone tissue engineering there is an enormous research activity focused on delivering new and improved bio-mimetic materials. The level of biological complexity that needs to be recapitulated within a synthetic three-dimensional environment is still uncertain. This requires the importance of close interaction between the surgical and cell biology communities. Advances in materials processing are also having a positive impact on the field. In the body, bone often has a structurally important interface with other tissues such as cartilage and ligament/tendon, for which designed scaffolds can be used to create tissue interfaces. Soft material routes like sol-gel processing might also be a strategy to incorporate bio-molecules during scaffold fabrication.

Coming

Conferences and Symposia

25TH INTERNATIONAL CONFERENCE ON LOW TEMPERATURE PHYSICS (LT25)

6–13 August 2008
Amsterdam, Netherlands
http://www.lt25.nl/

THE 13TH INTERNATIONAL CONFERENCE ON RAPIDLY QUENCHED AND METASTABLE MATERIALS

24–29 August 2008
Dresden, Germany
http://rq13.ifw-dresden.de/

14TH INTERNATIONAL CONFERENCE ON THE PHYSICS OF HIGHLY CHARGED IONS

1–5 September 2008
Chofu City Culture Hall "Tazukuri", Chofu, Tokyo, Japan
http://yebisu.ils.uec.ac.jp/hci2008

16TH INTERNATIONAL SYMPOSIUM ON BORON, BORIDES AND RELATED MATERIALS

7–12 September 2008
Matsue, Shimane, Japan
http://www.sogalabo.jp/ISBB2008/

INTERNATIONAL WORKSHOP ON STATISTICAL-MECHANICAL INFORMATICS 2008 (IW-SMI 2008)

14–17 September 2008
Aobayama, Aoba-ku, Sendai 980-0856, Japan
http://dex-smi.sp.dis.titech.ac.jp/DEX-SMI/iw-smi2008/

INHALED PARTICLES X

23–25 September 2008
Manchester University, UK
http://www.bohs.org/newsArticle.aspx?newsItem=61

HFM 2008 BRAUNSCHWEIG (HIGHLY FRUSTRATED MAGNETISM)

7–12 September 2008
Branschweig, Germany

AB INITIO SIMULATION OF CRYSTALLINE SOLIDS: HISTORY AND PROSPECTS

8–9 September 2008
Torino, Italy

THE 5TH INTERNATIONAL CONFERENCE ON RADIOTHERAPY GEL DOSIMETRY (DOSGEL 2008)

September 2008
University of Heraklion, Crete, Greece

INTERNATIONAL WORKSHOP ON POSITRON STUDIES OF DEFECTS (PSD '08 PRAGUE)

September 2008
Prague, Czech Republic

THE LXIII YAMADA CONFERENCE ON PHOTO-INDUCED PHASE TRANSITION AND COOPERATIVE PHENOMENA (PIPT3)

12–15 November 2008
Osaka, Japan

P. Nachtigall
E. Garrone
G. Turnes Palomino
M. Rodríguez Delgado
D. Nachtigallová
C. Otero Areán*

Institute of Organic Chemistry and Biochemistry, Academy of Sciences, Czech Republic
** dqueep0@uib.es*

FTIR Spectroscopic and Computational Studies on Hydrogen Adsorption on the Zeolite Li–FER

The interaction, at a low temperature, between molecular hydrogen and the zeolite Li–FER was studied by means of variable temperature infrared spectroscopy and theoretical calculations using a periodic DFT model. The adsorbed dihydrogen molecule becomes infrared active, giving a characteristic IR absorption band (H–H stretching) at 4090cm^{-1}. Three different Li+ site types with respect to H_2 adsorption were found in the zeolite, two of which adsorb H_2. Calculations showed a similar interaction energy for these two sites, which was found to agree with the experimentally determined value of standard adsorption enthalpy of ΔH_0=–4.1(±0.8)kJ.mol^{-1}. The results are discussed in the broader context of previously reported data for H2 adsorption on Na–FER and K–FER.

Keywords: *FTIR spectroscopy, Hydrogen adsorption,*
Received 4 January 2008, Revised 2 March 2008, Accepted 9 March 2008

1. Introduction

Studies of reversible gas adsorption on zeolites and related microporous materials are relevant to several technological processes, including gas separation (based on differential adsorption of different gases), gas sensing and storage. Hence, a detailed understanding of gas–solid interactions and quantification of the interaction energy is of interest, not only from the point of view of fundamental research, but also because practical applications would benefit from such studies. However, reversible gas adsorption involves only weak gas–solid interactions, typically within the range of 2–20 kJ mol^{-1}, which pose demanding requirements on both experimental measurements and theoretical calculations.

On the experimental side, it was recently shown [1-2] that variable temperature infrared spectroscopy is a convenient method to determine gas adsorption enthalpy when dealing with weak gas–solid interactions, and this method is applied here to the study of hydrogen adsorption (at low temperature) on the zeolite Li–FER. Detailed analysis of experimental data can be accomplished by means of a parallel theoretical investigation on the zeolite adsorption sites, the geometry of the adsorption complex, and the corresponding interaction energy. For this purpose, we have used a periodic density functional description which, by paying due consideration to the zeolite framework topology, gives a far more realistic description of the gas–solid interaction than that which can be obtained with simple cluster models.

Related studies on hydrogen adsorption at low temperature on Na–FER and K–FER were reported recently [3], so the results obtained for the H_2–Li–FER system can be analysed in a broader context. By doing so, further insight into the gas adsorption process can be gained, which constitutes an added aim of the present work. It should also be noted that hydrogen interactions with cations in mordenite and chabazite were recently studied by means of theoretical calculations by Benco *et al*. [4] and Solans-Monfort *et al*. [5] Detailed calculations for H_2 interactions with bare alkali metal cations were reported by Vitillo *et al*. [6].

2. Materials and Methods

2.1. Experiment

The ferrierite sample used in this study was supplied by the Research Institute of Inorganic Chemistry, Ústí nad Labem. It was in the ammonium form and had a nominal Si :Al ratio of 8.5 :1. From the parent zeolite, the lithium-exchanged sample was obtained by repeated ion exchange with a 0.5 M aqueous solution of LiCl. Powder X-ray diffraction of the exchanged sample showed good crystallinity, and all diffraction lines present in the diffractogram corresponded to the FER structure type. Complete ion exchange was checked by the absence of IR absorption bands corresponding to either the ammonium ion or the Brønsted acid Si(OH)Al group, which would be generated

during thermal activation (see below) of the zeolite sample if total exchange of the alkali metal ion for ammonium did not take place in the parent NH_4–FER material.

For IR spectroscopic measurements, a thin self-supported wafer of the zeolite sample was prepared and activated (outgassed) in a dynamic vacuum (residual pressure $<10^{-4}$ Torr) for 3h at 700 K inside an IR cell [7], which allowed *in situ* sample activation, gas dosage and variable temperature IR spectroscopy to be carried out. After running the blank spectrum of the zeolite wafer at 77 K, the cell was dosed with hydrogen, it was then closed and IR spectra were recorded at several fixed temperatures within the range of 79–150 K, while simultaneously registering sample temperature and hydrogen equilibrium pressure inside the cell. A platinum resistance thermometer and a capacitance pressure gauge were used for that purpose. The precision of these measurements was about ±2 K and ±2 × 10^{-2} Torr, respectively. Transmission FTIR spectra were recorded at 3 cm^{-1} resolution using a Bruker IFS66 spectrometer. In order to check reproducibility, and also to improve accuracy, after completing a first series of measurements the infrared cell was outgassed, dosed again with hydrogen, and a second series of spectra was recorded.

2.2. Calculations

The orthorhombic unit cell of ferrierite (I_{mmm} space group) contains 36 T atoms and 72 O atoms. The equilibrium volume of the all-silica FER unit cell fitted previously (cell parameters a=19.1468Å, b=14.3040Å and c=7.5763Å, volume 2076.70$Å^3$) [8] was used for all calculations on H_2–Li–FER. One framework Si atom was replaced by aluminium and the charge was compensated for by a Li^+ cation. Calculations of H_2 adsorption enthalpies were carried out for Li^+ in the vicinity of the Al atom in the T1, T2, and T3 positions (numbering scheme of Ref. [9]). Since substitution of one aluminium for one silicon atom only causes a negligible change in the unit cell volume, the geometries of Li–FER and H_2–Li–FER were optimized within the constraint of the unit cell parameters while all other degrees of freedom were fully relaxed.

Calculations were performed using the periodic DFT method, employing the Perdew–Burke–Erzerhofer (PBE) exchange–correlation functional [10-11] and the projector augmented wave approximation (PAW) of Blöchl, as adapted by Kresse and Joubert [12-13]. The plane wave basis set with a kinetic energy cut-off of 400 eV was used. Brillouin-zone sampling was restricted to the gamma-point. Calculations were performed using the VASP program [14-17].

Experimental determination of ΔH^0 was carried out at temperatures around 100K. To compare the calculated interaction energy (electronic interaction energy) with the experimental adsorption enthalpy value, it is necessary to include several corrections: the effect of ZPE, a thermal contribution, and the pV term. Zero-point energy (ZPE) corrections were calculated within the harmonic approximation. The effect of temperature ($\Delta U^0(100) - \Delta U^0(0)$) was evaluated from the partition function considering six degrees of freedom (see [3] for details). Thermal excitation of vibrational degrees of freedom was considered. The ideal gas equation was used for the transition from internal energy change to enthalpy change ($\Delta H^0(T) = \Delta U^0(T) + pV = \Delta U^0(T) + RT$).

The correction to the electronic interaction energy (calculated with the periodic DFT model) was evaluated for the 1-T cluster model ($Al(OH)_4^-M^+$ cluster), and this correction ($\Delta H^0(100K) - \Delta E^{el}(0K) = 4.9 kJ.mol^{-1}$) was used for all H_2 adsorption sites considered in Li–FER. A detailed description of this approach can be found in [3]. Calculations on cluster models were performed with the PBE exchange–correlation functional and with the aug-cc-pVTZ basis set [18]. Calculations with the atom-centered basis set were carried out with the Gaussian03 program suite [19]. C_{2v} symmetry constraints were applied in all calculations with cluster models and interaction energies were corrected for the basis set superposition error [20]. For comparison, the Li^+ bare metal cation (0-T model) was also considered.

3. Results

3.1. Variable temperature FTIR spectroscopy

Representative variable temperature FTIR spectra (in the H–H stretching region) of H_2 adsorbed on Li–FER are depicted in Fig.(1). A single H–H stretching band is seen, centred at 4090 cm^{-1}. The bathochromic frequency shift, from the gas phase value (4163cm^{-1}) of the Raman-active H–H stretching vibration of the free H_2 molecule, amounts to –73cm^{-1} for Li–FER. For comparison, H_2 adsorbed (at liquid nitrogen temperature) on the MFI-type zeolite Li–ZSM-5 was reported to give a single infrared absorption band at 4092cm^{-1} [21-22].

From the integrated intensity of variable temperature IR spectra, and by simultaneously measuring temperature and hydrogen equilibrium pressure, the standard adsorption enthalpy (ΔH^0) and entropy (ΔS^0) involved in the adsorption process were determined by using the VTIR method described in detail elsewhere.[1] Briefly, at

any given temperature, the integrated intensity of the IR absorption band should be proportional to surface coverage, θ, thus giving information on the activity (in the thermodynamic sense) of both the adsorbed species and the empty adsorbing sites; simultaneously, the equilibrium pressure does the same for the gas phase. Hence, the corresponding adsorption equilibrium constant, k, can be determined, and the variation of k with temperature leads to the corresponding values of adsorption enthalpy and entropy.

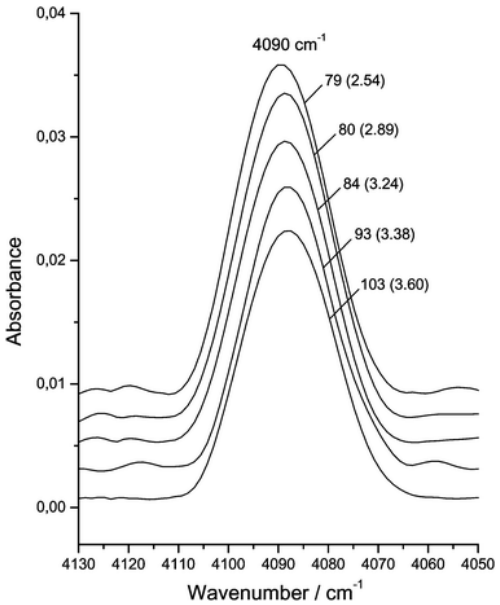

Fig. (1) Representative variable temperature FTIR spectra (zeolite blank subtracted) of H_2 adsorbed on Li–FER. Temperature, in K, and pressure (Torr, in brackets) as shown. For clarity the spectra have been offset on the vertical scale.

For deriving these values, integrated band intensity, A, temperature, T, and hydrogen equilibrium pressure, p, were considered to be interrelated by the Langmuir-type equation

$$\theta = A/A_M = k(T)\,p/[1 + k(T)\,p] \quad (1)$$

where A_M stands for the integrated intensity corresponding to full coverage. Combination of Eq. (1) with the well known van't Hoff equation, Eq. (2), gives Eq. (3) below:

$$k(T) = \exp[\Delta S^0/R]\,\exp[-\Delta H^0/RT] \quad (2)$$

$$\ln[A/(A_M - A)p] = (-\Delta H^0/RT) + (\Delta S^0/R) \quad (3)$$

from which ΔH^0 and ΔS^0 can be derived.

The plot of the left-hand side of Eq. (3) *versus* reciprocal temperature for all of the experimental measurements, depicted in Fig. (2), shows a good linear fit of Eq. (3). Note that the value of A_M needed (for which only an approximate estimation was known, since experimental points in Fig. (1) correspond to coverages far from saturation) was chosen as that giving the best linear fit of Eq. (3) for all experimentally determined points (see [1] for details). From this A_M value, it was inferred that experimental points in Fig. (2) correspond to a coverage range of $0.20 \le \theta \le 0.65$. From the linear plot in Fig. (2), the standard adsorption enthalpy was determined to be ($\Delta H^0 = -4.1$ kJ mol^{-1}) and the corresponding entropy change (ΔS^0) is (–57J.mol^{-1}.K^{-1}). The estimated error limits are about (±0.8kJ.mol^{-1}) for the enthalpy and (±10J. mol^{-1}.K^{-1}) for the entropy.

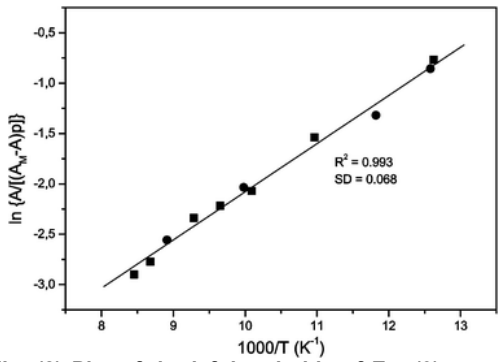

Fig. (2) Plot of the left-hand side of Eq. (3) *versus* reciprocal temperature for spectra measured in two independent runs (circle and square symbols). R, linear regression coefficient; and SD, standard deviation.

3.2. Computational study

The structure of cation sites and coordination of the Li^+ ion in FER was investigated systematically, considering all possible coordinations of the metal cation in the vicinity of each of four distinguishable framework aluminium atoms [23]. Two site types were found in the vicinity of a single framework Al atom: (i) channel wall site (denoted M7/T3) where Li^+ is located on top of a 6-membered ring on the channel wall, and (ii) intersection site (I2/T2) where Li^+ is located in the 8-membered entrance window of the perpendicular channel, at the intersection of the main and perpendicular channels. The interaction of H_2 with Li^+ cations in the zeolite was studied for the most stable Li^+ site of each type, M7/T3 and I2/T2. In addition, H_2 adsorption on the P6/T1 site, that has a rather peculiar geometry (the Li^+ ion is located right in the plane of the 6-membered window located at the bottom of FER cage) was also studied. The investigated sites are depicted in Fig. (3).

Results obtained with the periodic DFT model (FER) are reported in Table (1), along with those obtained using less sophisticated 0-T and 1-T cluster models. The strongest interaction (–23.5kJ.mol^{-1}) was found for H_2 adsorption on a bare Li^+ cation (0-T model). This is not surprising in light of previous theoretical work [5] which showed that the H_2 interaction with alkali metal cations is dominated by the polarization contribution. The interaction of H_2 with the Li^+ site represented by the 1-T model is five times weaker than interaction with the bare Li^+ cation. Calculations performed on the periodic model gave ΔH^0 values which are much

smaller than that for the bare cation (as expected), but they are comparable to, or even larger than, the adsorption enthalpy obtained with the 1-T cluster model.

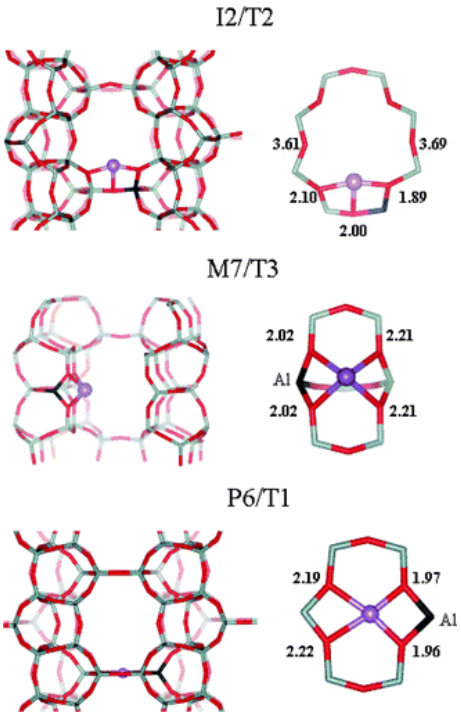

Fig. (3) The most stable Li^+ sites in FER. The localization of the site is depicted in the left part of the figure, viewed along the perpendicular, main, and perpendicular channel for the I2/T2, M7/T3, and P6/T1 site, respectively. The I2/T2 site is at the 8-membered entrance window of the perpendicular channel, on the intersection of both channels. The M7/T3 site is located in the main channel. The P6/T1 site is located in the plane of the 6-membered ring separating two adjacent FER cages. Details of Li^+ coordination for each site type are given in the right-hand side. Distances between the Li^+ ion and closest framework oxygen atoms are shown in Å.

The values of H_2 adsorption enthalpy on the Li^+ cation at the intersection site (I2/T2) were –5.6 and –5.9kJ.mol^{-1} for the H_2 molecule approaching the Li^+ ion from the main and the perpendicular channel, respectively. It is apparent that two H_2 molecules can interact with one Li^+ at the intersection site (Fig. (4a)) at the same time without affecting each other. The H_2 adsorption enthalpy on the Li^+ cation at the channel wall site (M7/T3) is slightly smaller (by about 1kJ.mol^{-1}) than that for the intersection site. However, H_2 cannot be adsorbed on the Li^+ ion at the P6/T1 site.

For all models investigated (0-T, 1-T, and periodic model), the structures having the lowest energy were T-shaped adsorption complexes. The H–H bond length is elongated by only a few thousandths of an Å upon interaction with the alkali metal cation. (Note that in the gas phase H_2 molecule r(H–H) is 0.751Åat the PBE level using both the aug-cc-pVTZ and plane-wave basis sets). The largest H–H bond length elongation is found for H_2 interacting with a bare Li^+ ion (almost 0.01Å), the smallest change in H–H bond length is observed for the least stable P6/T1 site. It is apparent from Table (1) that the calculated ΔH^0 values correlate with corresponding H–H bond elongation. The coordination of the metal cation to the zeolite framework was found to be unaltered upon interaction with adsorbed H_2.

Table 1 Adsorption enthalpy and bond distances for H_2 adsorbed on Li^+ cations, obtained with DFT calculations on cluster models (0-T and 1-T) and on the periodic model (FER)

Cluster model	H_2 Location[b]	r(H–H) /Å	r(Li–H) /Å	ΔH^0(100) /kJ mol^{-1}
0-T		0.7609	2.026	–23.5
1-T		0.7547	2.155	–4.7
FER[a]				
M7/T3 + H_2	M	0.7549	2.180, 2.204	–4.6
I2/T2 + H_2	M	0.7559	2.206, 2.235	–5.6
I2/T2 + H_2	P	0.7561	2.183, 2.195	–5.9
I2/T2 + 2 × H_2[c]	M	0.7554	2.207, 2.242	–5.2
	P	0.7561	2.220, 2.229	
P6/T1 + H_2[e]	P	0.7536	2.479, 2.434	0.1
Experimental value				–4.1 (±0.8)

[a] Alkali metal sites are defined in Fig. (1). [b] M and P denotes the H_2 molecule located in the main and in the perpendicular channel of FER, respectively. [c] Adsorption complex of two H_2 molecules on the I2/T2 site depicted in Fig. (4a). [d] Average adsorption enthalpy. [e] A positive value of ΔH^0(100) results from the use of constant correction (ΔH^0(100K)–ΔE^{el}(0K) =4.9kJ.mol^{-1}) for all sites.

4. Discussion

The experimentally determined value of ΔH^0=–4.1kJ.mol^{-1} is close to the corresponding values calculated using the periodic DFT approach (Table (1)), excluding site P6/T1 which should not contribute to hydrogen adsorption. It should be noted, however, that the excellent agreement found between experimental and calculated values of standard adsorption enthalpy could, to some extent, be fortuitous. Two main sources of uncertainty can affect calculated ΔH^0 values. First, the interaction energy calculated using GGA functionals (including the PBE functional) is known to be somewhat overestimated, while attraction due to dispersion forces is neglected at the DFT level, so these two terms can partially cancel out calculation errors. Secondly, the thermal contribution to ΔU^0(100)

was calculated from the vibrational partition function of the adsorption complex, using frequency values obtained at the harmonic approximation for the 1-T cluster model, and it is worth noticing that this approximation can be rather inaccurate, particularly for low lying vibrational modes. In addition, use of the 1-T cluster model neglects interaction of the H_2 molecule with the zeolite channel wall. More refined calculations, however, would require a degree of complexity which is well beyond the scope of the present work.

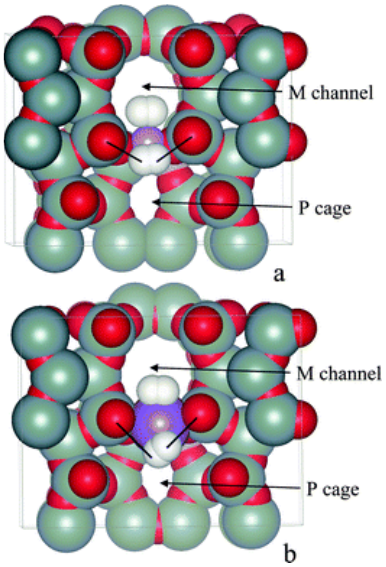

Fig. (4) Adsorption complexes of two H_2 molecules on (a) Li^+ and (b) Na^+ cations at the I2/T2 intersection site (viewed along the main channel). The nearest framework oxygen atoms are on average 2.91Å and 3.29Å away from hydrogen atoms in Li–FER and Na–FER zeolites, respectively.

Regarding multiplicity of adsorption sites, theoretical calculations have clearly shown that the H_2 molecule can be adsorbed on two different site types: the intersection site (I2/T2) and channel wall site (M7/T3). In addition, two different adsorption complexes (having either one or two adsorbed molecules) can be formed on the intersection site. By contrast, IR spectra show only a single infrared absorption band (Fig.(1)) and, in addition to that, the experimental data could be interpreted by assuming a single (homogeneous) adsorbing site, *i.e.*, within the context of an ideal Langmuir behaviour, which is implicit in Eq. (3). These seemingly contrasting results can be reconciled by noticing that differences in the interaction energy for individual adsorption sites are not greater than 1.3kJ.mol^{-1}, so (i) these differences are too small to cause a significant deviation from the ideal Langmuir behaviour, and (ii) IR spectroscopy (at 3cm^{-1} resolution) cannot resolve infrared absorption bands originating from the different adsorption complexes formed in the H_2–Li–FER system.

As already mentioned in the Introduction, a comparison of results obtained in this study with previously reported data [3] for the H_2–Na–FER and H_2–K–FER systems is of interest. Table (2) summarizes experimentally determined values for the three gas–solid systems. The bathochromic frequency shift, $\Delta\nu$, is seen to follow a homogeneous trend (as expected), being largest for H_2 adsorbed on Li–FER and smallest for K–FER. However, the adsorption enthalpy, ΔH^0, does not follow the same trend: for the H_2–Li–FER system, the corresponding value (–4.1 kJ.mol^{-1}) is lower than that found for the H_2–Na–FER system (–6.0kJ.mol^{-1}). This somewhat puzzling observation finds a precedent in previously reported studies [21,24] on H_2 adsorption on alkali metal exchanged ZSM-5 zeolites. For H_2–Li–ZSM-5, reported values of $\Delta\nu$ and ΔH^0 are –71cm^{-1} and –6.5kJ.mol^{-1}, respectively, while for H_2–Na–ZSM-5 they are –62cm^{-1} and –10.3kJ.mol^{-1}. It should also be noted that, in agreement with experimental results, the calculated adsorption enthalpy of H_2 on Li–FER (–4.6 to –5.9 kJ mol^{-1}, Table (1)) is smaller than that found[3] for H_2 on Na–FER (–5.2 to –7.0 kJ mol^{-1}). A tentative explanation for the H_2–Li–ZSM-5 system showing a larger $\Delta\nu$ value than H_2–Na–ZSM-5, while ΔH^0 is smaller for H_2–Li–ZSM-5 than for H_2–Na–ZSM-5, was given in Ref. [21]. Some of us proposed that, upon coordination to the adsorbed H_2 molecule, the Li^+ ion could slightly move outward from its original position on the zeolite wall, so as to optimize the interaction with the adsorbed molecule. Since this step would (necessarily) be endothermic, the overall value of ΔH^0 would be lower than expected as compared to the H_2–Na–ZSM-5 system. However, no theoretical calculations were performed at the time to substantiate this tentative hypothesis. We now report calculations for alkali metal exchanged ferrierite which give some evidence that cation movement is not a major reason for a low value of the adsorption enthalpy of H_2 on Li^+ sites.

Table 2 Experimentally determined data for H_2 adsorption on Li^+, Na^+ and K^+ exchanged ferrierite

	ν^{a}/cm^{-1}	$\Delta\nu^{b}$/cm^{-1}	$\Delta H^0(100)^{c}$/kJ mol^{-1}
Li–FER[d]	4090	–73	–4.1 (±0.8)
Na–FER[e]	4100	–63	–6.0 (±0.8)
K–FER[e]	4111	–52	–3.5 (±0.8)

[a] H–H stretching wavenumber of adsorbed H_2. [b] Bathochromic shift from 4163 (free H_2). [c] Standard adsorption enthalpy. [d] Present work. [e] Results from a parallel study on Na–FER and K–FER [3]

The calculated energy terms and geometric parameters of Li^+, Na^+ and K^+ interaction with the framework and the adsorbed H_2 molecule are summarized in Table (3). Results obtained for the I2/T2 site are shown, together (for comparison) with corresponding values for the 1-T cluster model. Note that the H_2 electronic interaction energy (ΔE_{el}) calculated with the 1-T cluster model decreases monotonically from Li^+ to K^+, as expected from simple electrostatic considerations. However, at the periodic DFT level the electronic interaction energy is the same for H_2 adsorbed on Li^+ and Na^+ sites. Upon accounting for the effect of the vibrational zero-point energy and thermal corrections, the H_2 interaction with the Na^+ site becomes stronger than that for the Li^+ site, while the H_2 interaction with the K^+ site is the weakest.

Table 3 Comparison of geometric and energy parameters for H_2 adsorption on Li^+, Na^+ and K^+ cations, calculated with the 1-T cluster model and the periodic DFT model for the I2/T2-P intersection site (H_2 molecule located in the P channel)

	Li^+	
	1-T	I2/T2
ΔE_{el}[a]/kJ mol^{-1}	−9.6	−10.8
ΔH^0 (100)[b]/kJ mol^{-1}	−4.7	−5.9
ΔE_{deform}[c]/kJ mol^{-1}	0	0.9
Δr(M–O)[d]/Å	0.01	0.02
r(M–H)/Å	2.16	2.19
r(M–O)[e]/Å	1.79	1.91
	1.79	2.01
		2.17
	Na^+	
	1-T	I2/T2
ΔE_{el}[a]/kJ mol^{-1}	−6.9	−10.8
ΔH^0 (100)[b]/kJ mol^{-1}	−3.2	−7.0
ΔE_{deform}[c]/kJ mol^{-1}	0	0.1
Δr(M–O)[d]/Å	0	0.01
r(M–H)/Å	2.58	2.45
r(M–O)[e]/Å	2.12	2.26
	2.12	2.48
		2.49
	K^+	
	1-T	I2/T2
ΔE_{el}[a]/kJ mol^{-1}	−2.6	−5.2
ΔH^0 (100)[b]/kJ mol^{-1}	−0.2	−2.8
ΔE_{deform}[c]/kJ mol^{-1}	0	0.1
Δr(M–O)[d]/Å	0	0
r(M–H)/Å	3.20	3.15
r(M–O)[e]/Å	2.48	2.87
	2.48	*2.90*
		3.23
		3.29

[a] Electronic interaction energy. [b] H_2 adsorption enthalpy. [c] Zeolite deformation energy is defined as the energy difference between the M–FER system energy at the geometry of the H_2–M–FER adsorption complex and at the equilibrium geometry of bare M-FER. [d] Average change of metal oxygen distance upon the interaction with H_2. [e] Distance between the metal cation and adjacent framework oxygen atoms, distance to O atom that is not part of AlO_4 tetrahedron in italic.

In order to examine whether the suprisingly small H_2 adsorption enthalpy on Li–FER is due to a cation displacement (leading to an endothermic step), the geometrical changes and corresponding framework deformation energy are also reported in Table (3). It is clear that there are only very small changes in the cation to framework oxygen distance (0.02 and 0.01Å for Li–FER and Na–FER, respectively). In addition, the framework deformation energy (defined as the difference between the M–FER system energy at the geometry of the H_2–M–FER adsorption complex and at the equilibrium geometry of bare M-FER) is only 0.9 and 0.1 kJ mol^{-1} for Li–FER and Na–FER, respectively. This suggests that the endothermic step is not contributing much to the overall adsorption enthalpy for these systems. However, it should be noted that for strongly adsorbed molecules, the framework deformation energy significantly lowers the adsorption enthalpy, as shown recently for CO and NO adsorption on Cu–ZSM-5 [25].

The Li^+ ion is tightly coordinated to oxygen atoms of the zeolite framework, as shown in Fig. (4). The geometrical parameters of H_2–M–FER complexes (M = Li and Na) are shown in Table (3). Note that going from the 1-T cluster model to the periodic model the M–H distance increases slightly in the Li^+ complex, while for the Na^+ complex it shortens by over 0.1Å. In agreement with this observation, the calculated H_2 adsorption enthalpy on Li^+ and Na^+ cations was found to increase by 0.9 kJ mol^{-1} (Table (1)) and 3.8 [3] kJ mol^{-1}, respectively, on going from the 1-T cluster model to the periodic FER model.

Fig. (4) depicts the adsorption complexes formed by two H_2 molecules in Li–FER and Na–FER (I2/T2 site). For Li–FER the adsorbed H_2 molecule comes significantly closer to adjacent framework oxygen atoms than for Na–FER. Average distances between H atoms and closest framework oxygens (shown by black segments in Fig. (4)) are 2.91Å for Li–FER and 3.29Å for Na–FER. Calculations of pair-interaction energy between H_2 and the zeolite framework (at the geometry of the corresponding adsorption complex) gave –0.7 and –1.9 kJ mol^{-1} for H_2–Li–FER and for H_2–Na–FER, respectively. Considering uncertainties inherent to the calculations performed, these energy values are too small to be confidently discussed. In addition, the H_2 interaction with the framework for other Li^+ and Na^+ sites in FER was found to be even smaller. Therefore, the reason for the enthalpy of adsorption of H_2 on Li–FER being smaller than that on Na–FER remains unclear. However, the above calculations suggest that, (i) deformation of the adsorption site upon H_2

coordination to the Li^+ ion is not the major factor involved, (ii) tight Li^+ coordination to the zeolite framework lowers the Li^+ ability to bind H_2, and (iii) H_2 interaction with the zeolite framework (at the equilibrium distance in the adsorption complex) could slightly stabilize the H_2–Li–FER and H_2–Na–FER complexes to different extents. Further studies seem to be desirable in order to shed light on these points.

5. Conclusions

The standard adsorption enthalpy of H_2 on the zeolite Li–FER was experimentally determined to be ΔH^0=–4.1(±0.8) kJ.mol^{-1} by means of variable temperature IR spectroscopy. This value was found to agree within ±1.5kJ.mol^{-1} with that calculated by using a periodic DFT method. However, such a close agreement can (in part) be due to internal cancellation of errors in the theoretical calculations.

Periodic DFT calculations showed that two different cation sites can adsorb hydrogen. One of them (M7/T3) is situated on the channel wall, the other (I2/T2) is at the intersection of two perpendicular channels. Only one H_2 molecule can be adsorbed on the M7/T3 site, while two H_2 molecules can be simultaneously adsorbed on the I2/T2 site. In both cases, the adsorption complex formed is T-shaped and the corresponding values of interaction energy are very similar. H_2 cannot be adsorbed on the P6/T1 site, where the Li^+ cation is located in the plane of a 6-membered ring separating adjacent FER cages.

Finally, it is worth noting that both DFT calculations and experimental results showed that the standard adsorption enthalpy of molecular hydrogen on Li–FER is about (1.5–2) kJ.mol^{-1} smaller than that on Na–FER. By contrast, the bathochromic frequency shift (from the free molecule value of 4163cm^{-1}) of the adsorbed H_2 molecule is larger for H_2–Li–FER than for H_2–Na–FER, with values of –73cm^{-1} and –63cm^{-1}, respectively.

References

[1] E. Garrone and C. Otero Areán, *Chem. Soc. Rev.*, 34, 2005, 846–857.

[2] C. Otero Areán *et al.*, *Phys. Chem. Chem. Phys.*, 4, 2002, 5713–5715.

[3] C. Otero Areán *et al.*, *J. Phys. Chem. B*, 110, 2006, 395–402.

[4] L. Benco *et al.*, *J. Phys. Chem. B*, 109, 2005, 22491–22501.

[5] X. Solans-Monfort *et al.*, *J. Phys. Chem. B*, 108, 2004, 8278–8286.

[6] J.G. Vitillo *et al.*, *J. Chem. Phys.*, 122, 2005, 114311.

[7] C. Otero Areán *et al.*, *Eur. J. Inorg. Chem.*, 2001, 7, 1739–1743.

[8] M. Bludsky *et al.*, *J. Phys. Chem. B*, 109, 2005, 9631–9638.

[9] P. A. Vaughan, *Acta Crystallogr.*, 21, 1966, 983.

[10] J. P. Perdew, K. Burke and M. Ernzerhof, *Phys. Rev. Lett.*, 77, 1996, 3865–3868.

[11] J. P. Perdew, K. Burke and M. Ernzerhof, *Phys. Rev. Lett.*, 78, 1997, 1396–1396.

[12] P. E. Blochl, *Phys. Rev. B*, 50, 1994, 17953–17979.

[13] G. Kresse and D. Joubert, *Phys. Rev. B*, 59, 1999, 1758–1775.

[14] G. Kresse and J. Hafner, *Phys. Rev. B*, 48, 1993, 13115–13118.

[15] G. Kresse and J. Hafner, *Phys. Rev. B*, 49, 1994, 14251–14269.

[16] G. Kresse and J. Furthmuller, *Comput. Mater. Sci.*, 6, 1996, 15–50.

[17] G. Kresse and J. Furthmuller, *Phys. Rev. B*, 54, 1996, 11169–11186.

[18] T. H. Dunning, *J. Chem. Phys.*, 90, 1989, 1007–1023.

[19] D. E. Woon and T. H. Dunning, *J. Chem. Phys.*, 98, 1993, 1358–1371.

[20] S. F. Boys and F. Bernardi, *Mol. Phys.*, 19, 1970, 553.

[21] G. Turnes Palomino *et al.*, *Stud. Surf. Sci. Catal.*, 158, 2005, 853–860.

[22] C. Otero Areán *et al.*, *Chem. Phys. Lett.*, 370, 2003, 631–635.

[23] R. Bulanek and P. Nachtigall, *Appl. Catal., A*, 307(1), 2006, 118-127.

[24] C. Otero Areán *et al.*, *Microporous Mesoporous Mater.*, 80, 2005, 247–252.

[25] M. Davidova *et al.*, *J. Phys. Chem. B*, 107, 2003, 2327–2332.

[26] M. Davidova *et al.*, *J. Phys. Chem. B*, 108, 2004, 13674–13682.

This article was reviewed at Department of Physics, University of Kuopio, FINLAND and School of Applied Sciences, University of Technology, Baghdad, IRAQ

Optical-Nose Technology Competes with Breathalyzers and Blood Tests

Written by
C. Kumar Patel
Eric Mueller

To many, the term "breathalyzer" conjures up images of flashing red lights, sobriety checkpoints, judges, and jail. But to someone involved with dialysis, either as a patient or practitioner, the term may soon connote rapid diagnosis, improved results, decreased cost, improved quality of life, and extended life span.

The lung-blood barrier is transparent to many small molecules. When we inhale, oxygen passes through the lung directly into the bloodstream, and when we exhale, carbon dioxide is expelled. In addition to these gases, expired breath contains a rich mixture of many other gases at parts-per-billion (ppb) levels, which not only can be quantitatively correlated with the amounts of the same gases in the bloodstream, but with concentrations of other molecules as well.

The presence of trace amounts of ammonia, nitric oxide, aldehydes, and ketones in the expired breath has been linked to kidney/liver malfunction, asthma, diabetes, cancer, and ulcers. The presence of carbon disulfide, ethane, butane, and pentane has been linked to neurological disorders. Consequently, the ability to rapidly, accurately, and noninvasively determine the level of these gases in a patient's breath *in situ* and in real time can have a profound impact on diagnosis, treatment, and end results. For example, during dialysis, monitoring the level of ammonia in the breath of a patient with renal failure can determine the level of blood urea nitrogen (BUN) at the start of and during the process, and can accurately indicate when the cleansing process is complete.

Pranalytica has developed ultrasensitive, laser-based, trace-gas detection technology (named O-Nose for optical nose) and instrumentation to enable noninvasive, real-time, and cost-effective diagnosis of a variety of vital human physiological functions. In addition to medical applications, the technology can be used in an industrial environment to monitor ambient air for the presence of contaminating, toxic, and explosive substances.

Detection technology

The detection technology uses photoacoustic spectroscopy, an absorption-based diagnostic tool, to detect and measure ppb concentrations of trace gases in expired breath. In brief, photoacoustic spectroscopy involves four steps (see Fig. 1): modulating the laser radiation, either in frequency or amplitude, at a wavelength that overlaps with a spectral feature of the target molecule; exciting the target molecule by absorption of the incident radiation; deactivating the excited molecule via collisions, during which the absorbed radiation energy is converted into periodic local heating at the modulation frequency; and monitoring the resulting acoustic waves with a microphone.

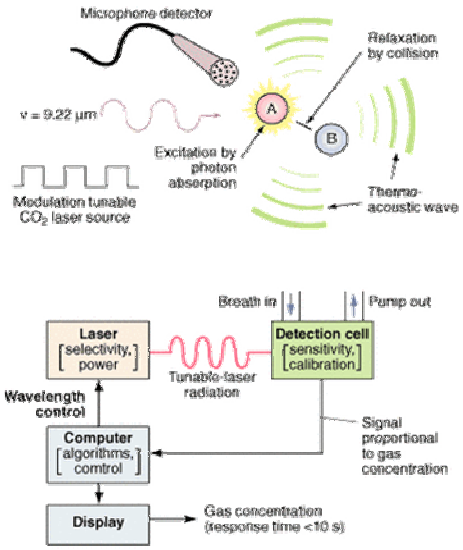

Figure (1) The photoacoustic process (top) is implemented by the O-Nose platform (bottom) in which the computer determines the appropriate wavelength for the target species and adjusts the laser to the appropriate spectral line. The patient breathes into a mask or tube connected to the calibrated acoustic detection cell, and the microphone detector picks up and amplifies the acoustic pressure wave generated by the relaxing molecules. The output signal is directly proportional to the concentration of the target species in the laser beam. The signal is processed by the computer and the results are displayed on the screen. Response time is less than 60 seconds, basically the time it takes for the breath to pass through the inlet tube into the measurement chamber.

The conversion of heat input from incident laser radiation into acoustic waves is described by the wave equation:

$$\nabla^2 p - \frac{1}{c^2}\frac{\delta^2 p}{\delta^2 t} = -\frac{(\gamma - 1)}{c^2}\frac{\delta H}{\delta t}$$

where p is the pressure, H is the generated heat, and γ is the ratio of specific heats. When the heat input is constant, $\delta H/\delta t = 0$, no pressure wave is generated. Thus, the heat must be modulated, which requires that the laser radiation must be modulated, either in amplitude or frequency. The magnitude of the photoacoustic signal that results is described by

$S=CPN\Delta t\sigma S_m$

where C is a cell-specific constant, P is the incident laser power, N is the number density of absorbing molecules, σ is the absorption cross section of the transition that is being interrogated, Δt is the cycle period of the modulated radiation, and S_m is the sensitivity of the microphone. The Δt term indicates that, for nonresonant operation, the signal decreases with increasing modulation frequency. As a result, most nonresonant measurements are made with modulation frequencies between 10 and 100 Hz. Unfortunately, $1/f$ noise is also higher in this measurement regime. The cell-specific constant C is a function of cell geometry, measurement conditions, and the modulation frequency. For measurement cells that are used as acoustic resonators, signals at resonance are significantly larger than those for nonresonant operation, despite the inverse dependence from the Δt term. The amount of signal enhancement that occurs when the laser is modulated at a resonant frequency is determined by the quality factor Q, which is the resonant frequency f_0 normalized by the half width of the resonance profile, Δf:

$$Q = \frac{f_0}{\Delta f}$$

It is clear from the last two equations that doubling the laser power, the number of molecules of the target species in the optical path, the microphone sensitivity, or, in the case of near-resonant operation, the cavity Q doubles the output signal.

Stable, sealed CO_2 lasers

Grating-tuned carbon dioxide (CO_2) lasers have long been used in the laboratory for photoacoustic trace-gas detection because of their high output power and their ability to produce discrete wavelengths that are strongly absorbed by species such as ammonia, benzene, and ethylene. They operate at approximately 120 discrete wavelengths between 9 and 11 µm. The CO_2 laser is particularly useful for detecting ammonia because one of its laser lines near 9.22 µm is nearly coincident with one of ammonia's strongest spectral feature, the sR(5,K) multiplet. Despite these advantages, CO_2 lasers have not typically been incorporated into commercial gas-sensing equipment because of their size, power requirements, and lack of long-term stability when operating on a single spectral line. This situation has changed with the availability of sealed-off, low-power (<25W) grating-tunable CO_2 lasers with excellent spectral resolution and stability as well as a compact footprint that can be easily deployed in a medical or industrial package.

The Pranalytica platform uses a standard Coherent-DEOS CO_2 laser that has been modified to incorporate a software-tunable custom grating. The laser has undergone a wide variety of performance and reliability tests, including repeated cycling between spectral lines every 10 seconds for 9000 hours. In the system, the laser can operate without adjustment for more than 15,000 hours.

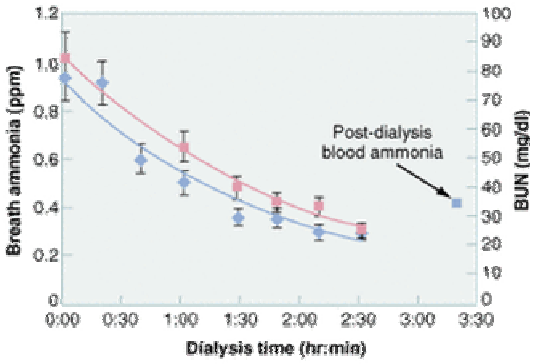

Figure (2) Breath ammonia and BUN measurements on one patient as a function of the dialysis time shows a 1:1 correlation between the BUN measurements and the breath ammonia measurements. The data are typical of the more than 20 patients already studied; therefore it appears that breath ammonia can be used as a real-time surrogate for BUN and creatinine data obtained through blood tests, which are generally available only 24 to 48 hours later.

The first laser breathalyzer

The O-Nose technology has been used to construct an instrument that measures ppb-level ammonia in expired human breath in the presence of a large number of other interfering species including >4% carbon dioxide and >10% water vapor. This instrument has been deployed in the kidney dialysis center at the University of California, Los Angeles, and in the obstetrics/gynecology center in the Olive View Medical Clinic in Sylmar, CA (see Fig. 2). Physicians and nurse practitioners at these sites use the instruments to collect clinical data on kidney dialysis patients and potential pre-eclampsia patients. Pre-eclampsia affects about 5% of pregnant women in their third trimester.

Comparison of breath and blood tests

Parameter	Breath test	Blood test
Skin puncture	No	Yes
Self-administration	Yes	No
Frequent	Yes	No
Continuous monitoring	Yes	No
Results	Immediate	12-48 hours
Cost	Low	Moderate
Patient and Physician feedback	Immediate	Delayed

An ongoing clinical study correlates breath ammonia measurements for kidney dialysis with simultaneously determined BUN and creatinine data obtained through taking blood samples (see Fig. 3). The advantages of breath tests over blood tests are numerous (see table, right). The breath-ammonia measurement protocol will provide the physician and the dialysis center staff with the real-time feedback needed to improve the quality of care given to the patient. In a home-dialysis environment, the technology promises the ability to assess simply the progress of dialysis and indicate to the patient when to stop a treatment session. This capability goes a long way toward ameliorating many of the serious quality-of-care issues voiced at the recent hearings by the U.S. Senate Subcommittee on Aging, and will provide an objective measure of the efficacy of the dialysis treatment.

Broad applications

The technology used for trace-gas detection is not limited to medical applications. Pranalytica recently introduced a trace-ammonia analyzer for industrial applications with a noise-limited detection sensitivity of ±0.2 ppb and an integration time of less than 30 seconds. The analyzer is destined for use in deep-UV submicron lithography applications where ambient ammonia concentration at levels as low as 10 ppb can be detrimental to the photoresists and impair the quality of the final product. The detection of this contaminant alone can save the foundries millions of dollars a year.

Another analyzer has been designed to detect gases other than ammonia. We are currently determining minimum sensitivity levels for a wide variety of industrial gases including hydrogen cyanide (<4 ppb), acetylene (<3 ppb), carbon monoxide (<650 ppb), and carbon dioxide (<55 ppm). Sub-ppb trace-gas analysis can also be used to detect explosives and chemical warfare agents such as nerve gases. This capability has immediate relevance to homeland security and battlefield applications.

In the semiconductor industry, the technology will have a significant role in maintaining the clean-room environment needed for the next generation of deep-UV lithography applications. And in the medical arena, noninvasive diagnostics with real-time point of care availability of the results is made possible by the marriage of photoacoustic spectroscopy to long-lived, stable, sealed, grating-tuned CO_2 lasers. This is likely to have a significant impact on health-care delivery and cost containment.

C. KUMAR N. PATEL *is a professor of physics at UCLA and chairman of the board at Pranalytica, 1101 Colorado Blvd., Santa Monica, CA 90401; e-mail: patel@pranalytica.com*

ERIC MUELLER *is manager of electro-optic engineering and systems at Coherent-DEOS, 1280 Blue Hills Ave., Bloomfield, CT 06002; e-mail: eric.mueller@coherentinc.com*

Adawiya J. Haider [1]
Khalil I. Hajem [2]
Mohammad K. Zaher [3]

[1] *School of Applied Sciences, University of Technology, Baghdad, IRAQ*
adawiya_haider@yahoo.com
[2] *Institute of Laser Postgraduate Studies, University of Baghdad, Baghdad, IRAQ*

Characterization of Diode Laser-Pumped Nd:YVO_4 Disk Laser

In this work describe experimental set up disk laser of Nd:YVO_4 in active mirror configuration, face pumping and cooling by thermoelectric Cooler (TEC) type heat exchanger to over come the limitation of prior design. With (4x5x1mm) disk dimensions to investigate the relationship between the pumping power from a diode laser at (808nm) with the optical elements in the setup and with the output power. The results show that a (0-600)mW CW output power which indicate 56% efficiency at (1064nm) wavelength from Nd:YVO_4 thin disk material when pumped with power between (0-1500) mW from a 808nm CW laser diode.

Keywords: Solid-state lasers, Active mirror, Nd:YVO_4 laser, Beam quality
Received 6 March 2008, Revised 2 May 2008, Accepted 9 May 2008

1. Introduction

Disk-type solid-state laser (SSL) has been recognized for its inherently low susceptibility to thermo-optical distortions, thermal lensing and stress birefringence [1]. Its large, round aperture reduces diffraction and beam clipping losses experienced by other SSL configurations. These attributes make the disk laser an attractive candidate for high-efficiency systems producing good quality beams. This type of laser is the subject of this work. The idea was proposed by Giesen in 1994. The attempts to use disk configuration is began before that where the early work on what called active mirror by General Electric Co. in 1968, Bert et al in 1974 [2].

In 1978, comparison study between the slab and disk configuration in parasitic oscillation, absorption was published [3]. Time resolved spectroscopy of flash lamp pumping a disk amplifier is studied by John H. Kelly et al in 1980 [4]. In 1981 J. A. Abate et al using Nd:glass material as disk laser called active mirrors, they operate it in high repetition rate as ignition device for controlled fusion experiments [2] in the same year David C. Brown et al gave the performance of active mirror amplifier in staging of both short pulse and long pulse for Nd:glass material using different configurations (split, sandwich) [5] .Also in 1981 J.H. Kelly et al gives the theoretical discretion of pumping system of the active mirror amplifier using a computer program called INVDEN to predict the performance of such system [6]. Eggleston *et al* presented detailed theoretical description of all the thermal effects in the slab geometry laser at first and then calculated these effects through computer program for Nd:YAG then they with 5Hz was the first high average power operation using Nd:Glass active mirror amplifier it was presented by David C. Brown et al 1n 1986 [7]. In 1994 Giesen et al opened the door for new configuration in the solid state laser called "the thin disk laser "to reach a high average power solid state laser pumped by diode array (HAP DPSSL) [3]. Lawrence Livermore National Laboratory (LLNL) and Boeing company through John Vetrovec and others published many papers in using and development this type of laser from 1997 to 2004 [8-28].

2. Laser Set-up

The schematic layout of the face pumped Nd:YVO_4 laser with a fiber-coupled diode laser is shown in Fig. (1). The laser diode driver "model *LDD1-1T-D*" has Thermo-Electric Controller and LCD display used to operate the laser diode unit with CW mode as shown in Fig. (2). Thermistors are useful for measuring temperature and gas flow or wind velocity. The laser diode is an 808nm, 2W laser diode with Single longitudinal mode Low threshold current 450mA. The optical fiber cable is diameter coupled to the laser diode .Optical and Electrical Characteristics of the laser diode is listed in the Table (1).

A two face dichroic mirror is used in the system. The first face mirror is high transparence for 808nm; the second face is anti reflection for 808nm high reflection for 1064nm at 45°.The crystal is of Nd:YVO_4 with (0.3at.%) doped with (4x5x1) mm dimensions placed on indium material of 0.1 mm thickness. In front of the disc is Al plate, and behind it there is a Cu plate those plates used as heat sink and 90% reflected mirror at 1064nm with ROC (200 mm).

Table (1) The optical and electrical characteristic of the laser diode

Parameter	Symbol	Min.	TYP.	Max.	Unit	Test Condition
Peak Wavelength	λ_p	805	808	811	nm	P=2W
Beam Divergence	$\Theta_{\parallel}$	6	8	10	Deg	FWHM
Beam Divergence	$\Theta_{\perp}$	12	16	20	Deg	FWHM
Operating Voltage	V_f		2.0	2.4	V	P=2W
Threshold Current	I_{th}		450	470	mA	CW
Operation Current	Iop		1.9	2	A	P=2W
Optical Output Power	P_0	2	Rating		W	
Case Temperature	T_0	12 - 35	Rating		°C	

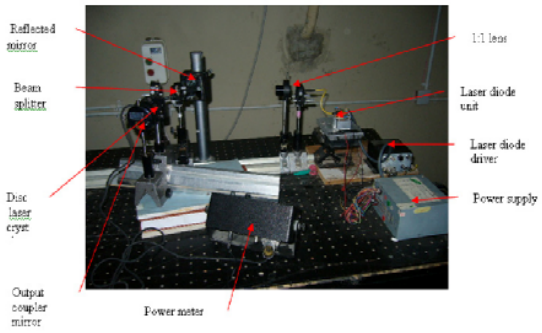

Fig. (1) Experimental setup of the diode pumped disc laser

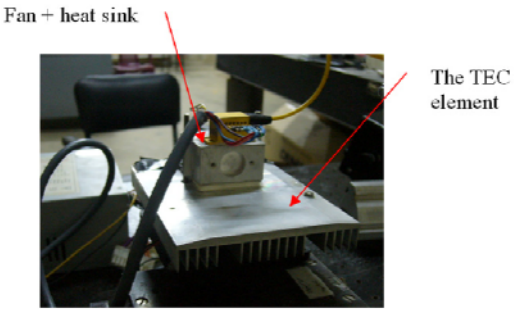

Fig. (2) The TEC element with laser diode. *Unit*

The beam radiated with 808nm from the laser diode is passed from the lens to focus on the disc crystal through the beam splitter. Laser beam of 1064nm, which radiated from the crystal is incident on the beam splitter then reflected on the output coupler mirror. A narrow band filter for 1064nm is used to test the output from the disc. An IR to visible converter is used to track the spot of laser in each point.

Fig (3) the schematic layout of the diode pumped Nd:YVO_4 laser with fiber coupled and presents the ray direction in the setup, where the lens on the disc crystal passing through the beam splitter focuses the laser from the diode, some of these rays are reflected out from the first surface so a high-reflected mirror is used to redirect that rays to the beam splitter and then to the disc. The output laser at 1064nm from the disc is reflected by high reflection surface of the rear face of the disc beam splitter towered the output coupler mirror. The out put beam at 1064nm is checked using a narrow band filter.

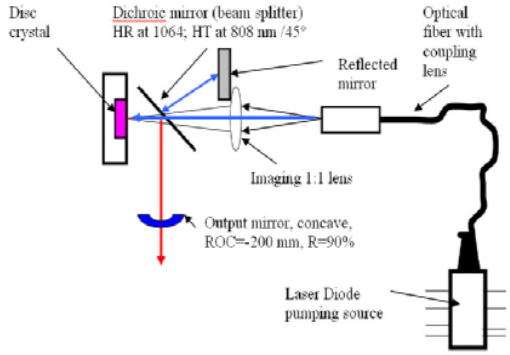

Fig. (3) The ray direction of the system

3. Experimental Results

A 2W laser diode with threshold of 325mA was used. The experimental curve of current-output of the laser diode is shown in Fig. (4). A GENETC power meter model (CE TPM 300, SP-310WB) is used to measure the out put power where it is placed 3cm away from the optical fiber because of the large divergence angle of the laser after the fiber.

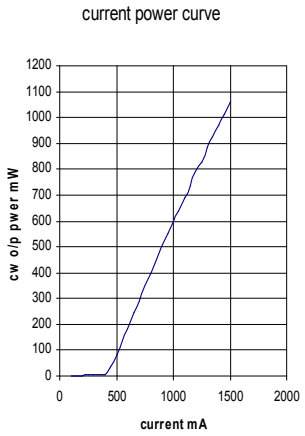

Fig. (4) Experimental calibration results

The results of the measuring power at each step in the set up in Fig. (3) as shown in Table (2) and can summarizes the following

- The threshold current is about 350mW

- The power of the laser diode decreases with about 8% this was found by dividing the value of the power before and after the lens.
- We found that there are some reflected beams from the beam splitter because the inaccuracy in determining the (45 degree) angle which is required for the beam splitter, so we used a reflected mirror to redirect this reflected beam to the beam splitter .The effects of the reflected mirror can be shown in Fig. (5)
- The whole optical loss from the lens to the laser disc crystal is about 0.72%. This is shown in Fig. (6)
- The CW output power from the disc is (600mW) and the optical efficiency is about 56% this is calculated by taken the slope between the absorbed powers after the beam splitter to the out put power after the out put coupler mirror as shown in Fig. (7)

Table (2) the results of the measuring power at each step in the setup

Current (mA)	Direct (mW)	Corrections Factor	After lens	Power after beam splitter without reflected mirror	Power after beam splitter with reflected mirror	O/P Power without Reflected Mirror	O/P Power with Reflected Mirror
100	0	0	0	0	0	0	0
150	2	2.857143	2.285714	1.782857	2.057143	0.980571	1.131429
200	2	2.857143	2.285714	1.782857	2.057143	0.980571	1.131429
250	4	5.714286	4.571429	3.565714	4.114286	1.961143	2.262857
300	4	5.714286	4.571429	3.565714	4.114286	1.961143	2.262857
350	4	5.714286	4.571429	3.565714	4.114286	1.961143	2.262857
400	5	7.142857	5.714286	4.457143	5.142857	2.451429	2.828571
450	36	51.42857	41.14286	32.09143	37.02857	17.65029	20.36571
500	82	117.1429	93.71429	73.09714	84.34286	40.20343	46.38857
550	136	194.2857	155.4286	121.2343	139.8857	66.67886	76.93714
600	185	264.2857	211.4286	164.9143	190.2857	90.70286	104.6571
650	247	352.8571	282.2857	220.1829	254.0571	121.1006	139.7314
700	293	418.5714	334.8571	261.1886	301.3714	143.6537	165.7543
750	347	495.7143	396.5714	309.3257	356.9143	170.1291	196.3029
800	400	571.4286	457.1429	356.5714	411.4286	196.1143	226.2857
850	450	642.8571	514.2857	401.1429	462.8571	220.6286	254.5714
900	498	711.4286	569.1429	443.9314	512.2286	244.1623	281.7257
950	550	785.7143	628.5714	490.2857	565.7143	269.6571	311.1429
1000	595	850	680	530.4	612	291.72	336.6
1050	640	914.2857	731.4286	570.5143	658.2857	313.7829	362.0571
1100	688	982.8571	786.2857	613.3029	707.6571	337.3166	389.2114
1150	733	1047.143	837.7143	653.4171	753.9429	359.3794	414.6686
1200	790	1128.571	902.8571	704.2286	812.5714	387.3257	446.9143
1250	825	1178.571	942.8571	735.4286	848.5714	404.4857	466.7143
1300	885	1264.286	1011.429	788.9143	910.2857	433.9029	500.6571
1350	926	1322.857	1058.286	825.4629	952.4571	454.0046	523.8514
1400	972	1388.571	1110.857	866.4686	999.7714	476.5577	549.8743
1450	1010	1442.857	1154.286	900.3429	1038.857	495.1886	571.3714
1500	1060	1514.286	1211.429	944.9143	1090.286	519.7029	599.6571

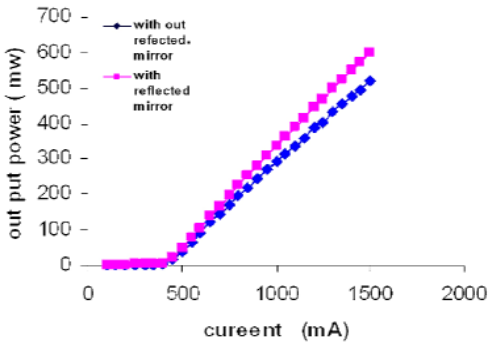

Fig. (5) The out put power V.S. current as a function the reflected mirror

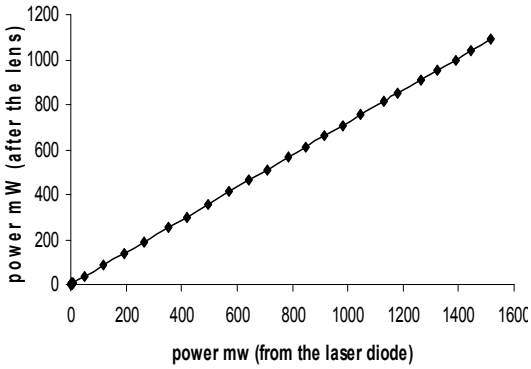

Fig. (6) Optical loss of the laser diode power

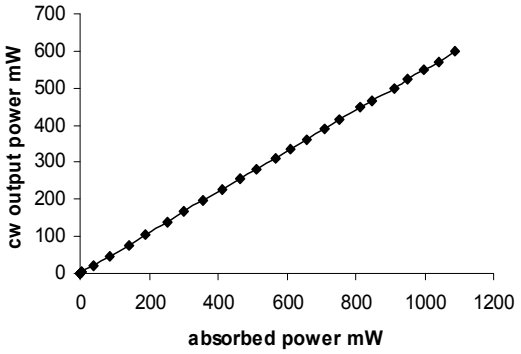

Fig. (7) The optical efficiency of the disc laser

4. Conclusion

For the experimental realization of the used disk laser of the present work an optical efficiency about 56% between the absorbed and output powers was achieved where a 600mW in CW operation was found.

References

[1] W. Koechner, **"Solid State Laser Engineering"**, Ch. 7, 5th edition, Springer-Verlag, NY, 1999.
[2] J.A. Abate, L. Lund, D. Brown, S. Jacob, *Appl. Opt.*, Vol. 20, No. 2, 15 Jan 1981.
[3] J.H. Kelly *et al.*, *Appl. Opt.*, Vol. 19, No. 22, (1980).
[4] D.C. Brown, *IEEE J. Quantum Electron.*, Vol. QE-17, No. 9.
[5] J. Thomas *et al.*, *IEEE J. Quantum Electron.*, Vol. QE-21, No. 8 (1985).
[6] D.C. Brown, *Appl. Opt.*, Vol. 25, No. 5, (1986).
[7] G.F. Alch, *"The Heat Capacity Disk Laser"*, UCRL-JC- 130962 "LLNL" (1997).
[8] C. Honninger, *Appl. Phys. B*, Vol.65, 423-426 (1997).
[9] R.J. Beach, *"High average power diode pumped Yb:YAG laser"*, LLNL, UCRL-JC-133848 (1999).
[10] L. Zabata, *"Composite Thin Disk Laser Scaleable To 100KW Average Power Output and Beyond"*, LLNL, UCRL-JC-138786 (2000).
[11] J. Vetrovec, *"Diode-Pumped Active Mirror Amplifier For High Average Power"*, Paper No. 2704, Laser'2000 Conference, Albuquerque, December 4-8, (2000).
[12] J. Vetrovec, *"Active Mirror Amplifier For High-Average Power"*, Paper 4270-06 presented at the Photonics West Lase'2001 Conference, San Jose, CA, January 22-26 (2001).
[13] J. Vetrovec, *"Compact Active Mirror Laser (CAMIL)"*, Preprint of a paper # 4630-02 presented at the Photonics West Lase'2002 Conference, San Jose, CA, January 22-26, 2001.
[14] J. Vetrovec, *"Solid-State Laser Scalable to Ultrahigh-Average Power"*, Presented at the Solid-State and Diode Laser Technology Review, Albuquerque, NM, May 21-24.
[15] J. Vetrovec, *"Large Aperture Disk Laser for DEW Applications"*, Presented at the 4th Annual Directed Energy Symposium Huntsville, AL, November 1, 2001.
[16] J. Vetrovec, *"Ultrahigh-Average Power Solid-State Laser"*, Presented at the High-Power Laser Ablation Conference in Taos, NM, April 22-26, 2002 (SPIE vol. 4760).
[17] J. Vetrovec *et al.*, Solid-State Disk Laser for High-Average GCL/HPL Conference, Wroclaw, Poland, August 26-30, 2002.
[18] L.E. Zapata *et al.*, *"Yb Thin-Disk Laser Results"*, Solid State and Diode Laser Technology Review 2002, Albuquerque, New Mexico, June 3-6, (2002) UCRL-JC- 48425.
[19] J. Vetrovec, *"Short-Pulse Solid-State Laser"*, Solid State and Diode Laser Technology Review 2002, Albuquerque, New Mexico, June 3-6, (2002) UCRL-JC- 48348,(2002).
[20] J. Vetrovec *et al.*, *"Development of Solid-State Disk Laser for High-Average Power"*, SPIE LASE 2003 Conference, San Jose, CA, January 26-31 (2003).
[21] J. Vetrovec *et al.*, *"Progress in the Development of Solid-State Disk Laser"*, SPIE LASE 2004, 5332-26, Conference, San Jose, CA, January 25-30 (2004).
[22] H. Ineyan and C. Hoefer, *"End-Pumping Zigzag Slab Laser Gain Medium"*, US Patent 094, 279 (2006).
[23] W.S. Martin and J.P. Chernoch, **"Total Internal Reflection Laser Device"**, General Electric Co., US Patent 3, 633, 126 (4 Jan, 1972).
[24] R. Beach, *"Delivering Pump Light Into A Laser Gain Medium While Maintaining Access To The Laser Beam"*, US Patent 222, 872 (2006).
[25] S. Yamamoto, "High Power Continuous-Wave Operation Of Side-Pumped Yb:YAG Thin Disk Laser", *Opt. Soc. Am.* (2003).
[26] C. Stewen, *IEEE J. Selected Topics in Quantum Electron.*, Vol. 6, No. 4 (2000).
[27] H. Yanagisawa *et al.*, "Compact Single-Bar Side-Pumped Yb:Yag Thin-Disk Laser", *Opt. Soc. Am.* (2003).
[28] C. Stolzenburg *et al.*, *"Power Scalability of Thin Disk Lasers in Fundamental Mode Operation"*, Conf. on Lasers and Electro-Optics Europe (2005).

This article was reviewed at National Institute for Applied Optics (INOA), Florence, ITALY, College of Science, University of Nizwa, OMAN and School of Applied Sciences, University of Technology, Baghdad, IRAQ

Shigeki Umemura
Yasunori Okano
Yasuhiro Hayakawa
Masashi Kumagawa
Akira Hirata
Sadik Dost

Department of Materials Science and Chemical Engineering, Shizuoka University, Japan

Marangoni Convection Effect on the Melting of GaSb/InSb/GaSb Sandwich Structured Sample

Effect of Marangoni convection on the flow and melting of the GaSb/InSb/GaSb sandwich structured sample is studied by means of the numerical simulation. Thermal Marangoni convection enhances the melting of crystal near the free surface under the both normal and reduced gravity fields. The effect of solutal Marangoni convection on the flow field is smaller than that of thermal Marangoni convection under the normal gravity field because of the gravitational segregation.

Keywords: *Marangoni convection, Compound semiconductor, Liquid/solid interface shape*
Received 1 May 2008, Accepted 9 May 2008

1. Introduction

The compound semiconductor is widely used as a material of electrical and optical devices. Especially, the ternary compound semiconductor is very useful because change of the bandgap energy and lattice constant is possible to be controlled by adjusting the compositional ratio. InGaSb, one of the ternary semiconductors, is promising for detectors and thermo-photo-voltaic cells in the near-infrared region, and the substrate for growing thin films. However, it is very difficult to grow high quality InGaSb bulk inside crystals because of the large solidus-liquidus separation of InSb-GaSb phase diagram and segregation due to density difference between InSb and GaSb. As a fundamental study for growth of the InGaSb bulk crystal, the authors have previously carried out melting and solidification experiments on GaSb/InSb/GaSb sandwich structured samples [1].

The experiments were carried out under the microgravity by using the Chinese recoverable satellite and on the earth. It was found that melting near the lower wall was enhanced under the normal gravity field because the component with heavier and lower melting temperature, InSb, sinks to the lower part of the liquid. This experimental result was well explained by using the numerical simulation. However, only solutal natural convection convection was considered in the previous simulation [1].

In this study, numerical simulation is carried out considering not only solutal and thermal natural convections but also both Marangoni convections.

2. Numerical Simulation

Figure (1) shows the configuration for the analysis. A solid in a two-dimensional rectangular quartz ampoule was heated from the upper and lower walls, and melted.

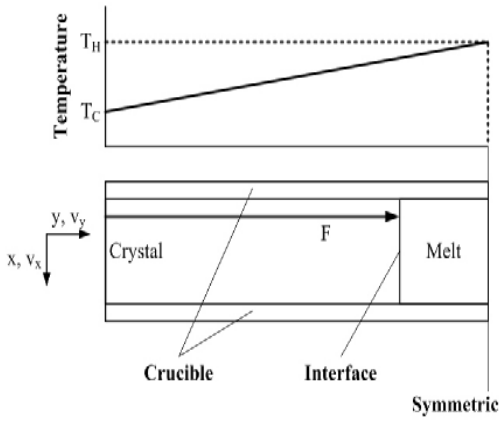

Fig. (1) Configuration for the analysis

The physical properties of GaSb in the crystal region and the InSb in the melt region were assumed. Temperatures along the both walls increase with time (1.0K/min) while keeping the temperature gradient constant (1.23×10^3K/m). The simulation model makes the following assumptions: (i) the liquid is incompressible and Newtonian, (ii) Boussinesq approximation, (iii) the change in volume and physical properties as a result of melting are negligible. Under these assumptions, the governing equations in the liquid are presented as follows:

$$\nabla . \vec{V} = 0 \qquad (1)$$

$$\frac{\partial \vec{V}}{\partial t} + \left(\vec{V}.\nabla\right)\vec{V} = -\frac{1}{\rho}\nabla p + v\left(\nabla^2 \vec{V}\right) - \vec{g}\beta_T \Delta T_l - \vec{g}\beta_C \Delta C_l \quad (2)$$

$$\frac{\partial T_l}{\partial t} + \left(\vec{V}.\nabla\right)T_l = \alpha \nabla^2 T_l \quad (3)$$

$$\frac{\partial C_l}{\partial t} + \left(\vec{V}.\nabla\right)C_l = D\nabla^2 C_l \quad (4)$$

The governing equation in the crystal and crucible is the following heat conduction equation:

$$\frac{\partial T_i}{\partial t} = \alpha_i \nabla^2 T_i \quad (5)$$

where $i = c$ or s

In equations (1-5), $\vec{V}$ is the velocity vector, t the time, ρ the density, p the pressure, v the kinematic viscosity, $\vec{g}$ the gravitational acceleration vector, α the thermal diffusivity, T the temperature, and D the diffusion coefficient. β_C and β_T are the solutal and thermal expansion coefficients, respectively. The subscript l, c and s are liquid, crucible and solid, respectively.

The effect of the Marangoni convection was considered in the following boundary conditions along free space:

$$\mu \frac{\partial V_y}{\partial x} = \mp\left\{\left(\frac{\partial \sigma}{\partial T}\right)\frac{\partial T_l}{\partial y} + \left(\frac{\partial \sigma}{\partial C}\right)\frac{\partial C_l}{\partial y}\right\} \quad (6)$$

where $\mp$ are changed whether the free surface position is upper or bottom of melt region; in the case of upper free surface, the sign of the equation is negative, and in the case of the bottom, the sign is positive.

The solid-liquid interface position is calculated by the following heat (Eq. 7) and mass (Eq. 8) balance equations along liquid/solid interfaces and the liquidus curve in the InSb-GaSb phase diagram.

$$\rho_s L \frac{\partial f}{\partial t} = \begin{Bmatrix} \lambda_s\left(\frac{\partial T_s}{\partial y} - \frac{\partial f}{\partial x}\frac{\partial T_s}{\partial x}\right) - \\ \lambda_l\left(\frac{\partial T_l}{\partial y} - \frac{\partial f}{\partial x}\frac{\partial T_l}{\partial x}\right) \end{Bmatrix}\left\{1 + \left(\frac{\partial f}{\partial x}\right)^2\right\} \quad (7)$$

$$C_l \frac{\partial f}{\partial t} = -D\left(\frac{\partial C_l}{\partial y} - \frac{\partial f}{\partial x}\frac{\partial C_l}{\partial x}\right)\left\{1 + \left(\frac{\partial f}{\partial x}\right)^2\right\} \quad (8)$$

In Eq. (7), L is the latent heat.

In order to relate these equations, the liquidus curve in the InSb-GaSb phase diagram [2] was correlated as follows:

$$C_i = -3.5896\times10^{-10}T_i^4 + 8.2758\times10^{-7}T_i^3 - 7.2136\times10^{-4}T_i^2 + 2.7746\times10^{-1}T_i - 38.325 \quad (9)$$

where C_i and T_i are the concentration and temperature along the liquid/solid interface

In order to treat curved interfaces, the boundary fixing method was adopted. The governing equations and boundary conditions were transformed into dimensionless forms, and discretized by the finite difference method. The discretized governing equations and boundary conditions were solved by the SOR (Successive Over Relaxation) method. The solution considering only thermal conductivity was used as initial state.

3. Results and Discussion

The Marangoni number is an important parameter to estimate the strength of Marangoni convection in the liquid. In this study, the following thermal (Ma_T) and solutal (Ma_C) Marangoni numbers are defined, respectively:

$$Ma_T = -\frac{\Delta TH\left(\frac{\partial \sigma}{\partial T}\right)}{\mu v} \quad (10a)$$

$$Ma_C = -\frac{\Delta CH\left(\frac{\partial \sigma}{\partial C}\right)}{\mu v} \quad (10b)$$

where σ and μ are surface tension and viscosity, respectively

The thermal and solutal Marangoni numbers corresponding to the previous experimental conditions [1] are given as $9.17\text{x}10^3$ and $1.60\text{x}10^6$. However, smaller Marangoni numbers were used in the present calculations to save computational time.

3.1 Under the normal gravity field

Figure (2) shows the effect of the Marangoni convection on the stream function (left half), concentration field (right field) and solid/liquid interface shape at t=50min. Figure (2a) shows the case where the free surface presents between the liquid and upper ampoule wall but no Marangoni convection is present, which corresponds to the case where only solutal natural convection is present in the liquid. Figure (2b) shows the case where the thermal Marangoni convection and solutal natural convection are present in the liquid, while Figure (2c) describes the case where the solutal Marangoni and natural convections are present. As shown in Fig. (2b), the thermal Marangoni convection induces the flow from the center to the crystal along the free surface. This flow direction is opposite to the flow due to the solutal natural convection, and the thermal Marangoni convection enhances the melting the upper part of the crystal.

As shown in Fig. (2c), the solutal Marangoni convection does not affect the flow field although the larger Marangoni number was used compared with the case of the thermal Marangoni convection. Because the behavior component, In-rich solution, sinks to the lower part of the liquid under the normal gravity field, concentration gradient along the free surface become very gentle. Consequently, strength of the flow induced by the solutal Marangoni

convection is very weak in spite of the large solutal Marangoni number.

The effect of Marangoni convection on the shape of the solid-liquid interface is shown in Fig. (3). As shown, the Marangoni convection enhances the melting near the free surface.

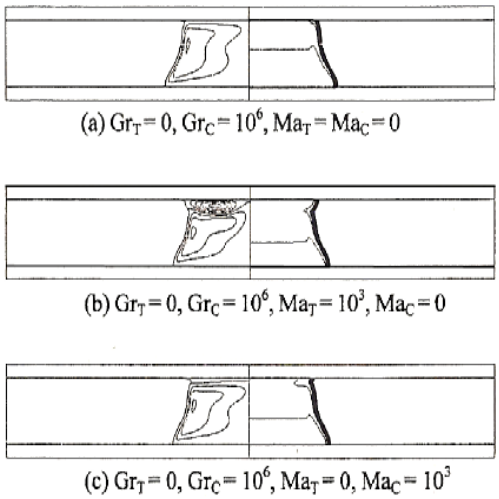

Fig. (2) Stream function (left half) and concentration (right half) on the earth (50min)

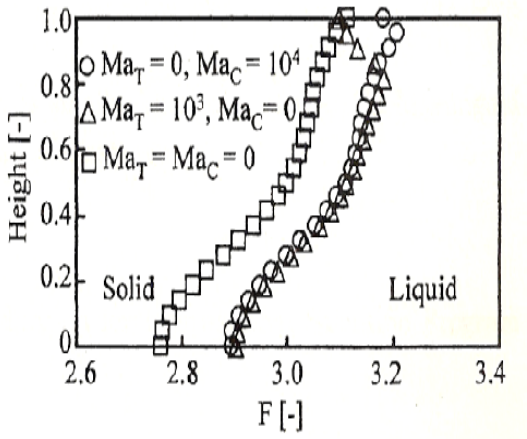

Fig. (3) Effect of Marangoni convection on the solid-liquid interface shape on the earth (50min)

3.2 Under the reduced gravity field

Figure (4) shows the effect of Marangoni convection on the stream function (left half), concentration field (right half) and solid/liquid interface shape at *t*=50min under the zero gravity field. There are two free surfaces along upper and lower walls. Fig. (4a) shows the case of no convection. In this case, the interface shape is almost flat and iso-concentration lines are parallel to the interface. Fig. (4b) describes the case where only thermal Marangoni convection is present in the liquid. The Marangoni convection enhances the melting near the free surfaces. Fig. (4c) shows the case where the thermal and solutal Marangoni convections are present in the liquid. Although the same Marangoni number is assumed, no remarkable difference between the Fig. (4b) and (4c) is recognized.

Figure (5) shows the value of maximum stream function when only thermal or solutal Marangoni convection is present in the liquid. Although the same Marangoni number is assumed, the maximum stream function due to the solutal Marangoni convection is much smaller than that due to the thermal Marangoni convection. It is found from Fig. (4) and (5) that the effect of solutal Marangoni convection is small in this experimental conditions.

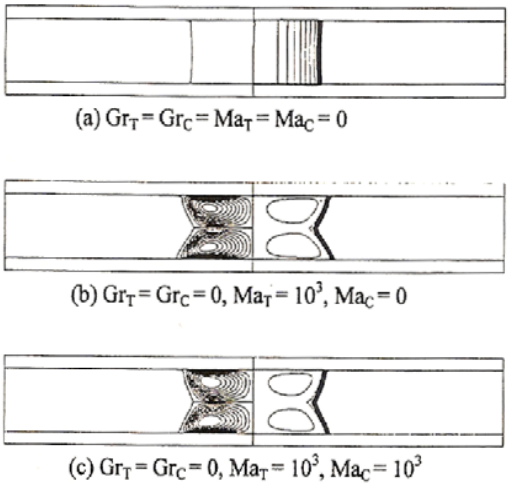

Fig. (4) Stream function (left half) and concentration (right half) under the no gravity field (50min) (Gr_T=Gr_C=0)

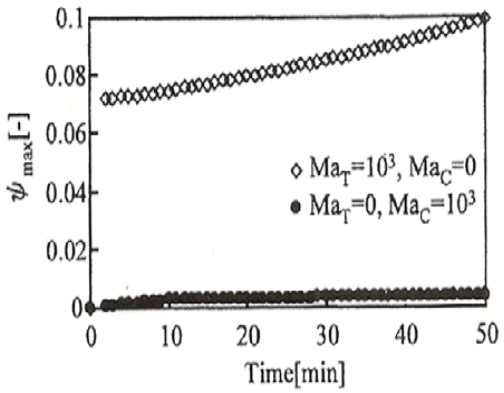

Fig. (5) Time dependency of the maximum stream function under the no gravity field (Gr_T=Gr_C=0)

4. Conclusion

In order to understand the effect of Marangoni convection on the melting process of GaSb/InSb/GaSb structured samples, a numerical simulation was carried out. We can conclude that thermal Marangoni convection enhances the

melting of crystal near the free surface under the both normal and reduced gravity fields. The effect of solutal Marangoni convection on the flow is smaller than that of thermal Marangoni convection under the normal gravity field because of gravitational segregation.

References

[1] Hayakawa, Y. et al., *J. Cryst. Growth*, 213 (1/2) (2000), 40.
[2] Stringfellow, G.B., *J. Phys. Solids*, 33 (1972), 665.

This article was reviewed at School of Applied Sciences, University of Technology, Baghdad, IRAQ

Coming Conferences and Symposia *Sponsored by SPIE*

SPIE Optics + Photonics
10 - 14 August 2008
San Diego, California, USA
Exhibition: 12 - 14 August 2008

NanoScience + Engineering, part of Optics+Photonics 2008
10 - 14 August 2008
San Diego, California, USA

Solar Energy + Applications, part of Optics+Photonics 2008
10 - 14 August 2008
San Diego, California, USA

Photonic Devices + Applications, part of Optics+Photonics 2008
10 - 14 August 2008
San Diego, California, USA

Optical Engineering + Applications, part of Optics+Photonics 2008
10 - 14 August 2008
San Diego, California, USA

SPIE Europe Optical Systems Design
2 - 5 September 2008
Glasgow, Scotland, UK
Exhibition: 3 - 4 September 2008

SPIE Europe Security + Defence
15 - 18 September 2008
Cardiff, Wales, UK
Exhibition: 16 - 17 September 2008

SPIE Europe Remote Sensing
15 - 18 September 2008
Cardiff, Wales, UK

Boulder Damage Symposium XL Annual Symposium on Optical Materials for High Power Lasers
22 - 24 September 2008
Boulder, CO, USA

SPIE Photomask Technology 28th Annual Symposium
6 - 10 October 2008
Monterey, California, USA
Exhibition: 7 - 8 October 2008

SPIE APOC 2008 Asia-Pacific Optical Communications
26 - 30 October 2008
Hangzhou, China

SPIE Lithography Asia - Taiwan
4 - 6 November 2008
Taipei, Taiwan

International Symposium on Optomechatronic Technologies
17 - 21 November 2008
San Diego, California, USA

SPIE Asia-Pacific Remote Sensing
17 - 21 November 2008
Noumea, New Caledonia

IRAQI JOURNAL OF APPLIED PHYSICS

" INSTRUCTIONS TO AUTHORS "

A new Iraqi specialized quarterly periodical dedicated to publishing original papers, letters and reviews in:

Applied & Nonlinear Optics	Electronic Materials & Devices	Quantum Physics & Spectroscopy
Applied Mechanics & Thermodynamics	Laser Physics & Applications	Semiconductors & Optoelectronics
Digital & Optical Communications	Plasma Physics & Applications	Solid State Physics & Applications

CONTRIBUTIONS

Contributions to be published in this journal should be original research works, i.e., those not already published or submitted for publication elsewhere, individual papers or letters to editor.

SUBMISSION OF MANUSCRIPTS

Manuscripts should be submitted to the editor at the mailing address:

Iraqi Journal of Applied Physics
Managing Editor
P. O. Box 55259, Baghdad 12001, IRAQ
irq_appl_phys@yahoo.com

Iraqi Journal of Applied Physics
Editor-In-Chief
P. O. Box 55159, Baghdad 12001, IRAQ
editor_ijap@yahoo.co.uk

MANUSCRIPTS

Two copies with soft copy on a compact disc (CD) should be submitted to Editor in the following configuration:

- Double-spaced one-side A4 size with 2.5 cm margins of all sides
- 12pt Times New Roman font
- Letters should not exceed 5 pages, papers no more 20 pages and reviews are up to author.
- Manuscripts presented in English only are accepted.
- Authors confirm affiliations, addresses and emails. Email is necessary for correspondences.
- English abstract not exceed 150 words
- 4 keywords (at least) should be maintained on (PACS preferred)
- Author(s) should express all quantities in SI units
- Equations should be written in equation form (italic and symbolic)
- Figures and Tables should be separated from text
- Figures and diagrams can be submitted in colors for assessment and they will be returned to authors after provide printable copies
- Charts should be indicated by the software used for
- Only original or high-resolution scanner photos are accepted
- References should be written in titles, full-name authors, names of publications, years, volumes, issues and pages (from-to)

PROOFS

Authors will receive proofs of papers and are requested to return one corrected hard copy with a WORD copy on a compact disc (CD). New materials inserted in the original text without Editor permission may cause rejection of paper.

COPYRIGHT FORM

Author(s) will be asked to transfer copyrights of the article to the Journal soon after acceptance of it. This will ensure the widest possible dissemination of information.

OFFPRINTS

Authors will receive offprints free of charge and any additional offprints can be ordered.

SUBSCRIPTION AND ORDERS

Annual fees (4 issues per year) of subscription are:

50 000 Iraqi dinars for individuals and establishments inside Iraq.
50 US$ for individuals and establishments abroad.

Fees are reduced by 25% for I.S.A.R.E.S.T. members. Orders of issues can be submitted by contacting the editor-in-chief or editorial secretary to maintain the address of issue delivery and payment way.

THE IRAQI JOURNAL OF APPLIED PHYSICS
EDITORIAL BOARD
P. O. Box 55259, Baghdad 12001, IRAQ
Email: editor_ijap@yahoo.com

COPYRIGHY RELEASE

Iraqi Journal of Applied Physics (IJAP)

We, the undersigned, the author/authors of the article titled

……
……
……
……
……
……

that is presented to the Iraqi Journal of Applied Physics (IJAP) for publication, declare that we have neither taken part or full text from any published work by others, nor presented or published it elsewhere in any other journal. We also declare transferring copyrights and conduct of this article to the Iraqi Journal of Applied Physics (IJAP) after accepting it for publication.

The authors will keep the following rights:

1. **Possession of the article such as patent rights.**
2. **Free of charge use of the article or part of it in any future work by the authors such as books and lecture notes without referring to the IJAP.**
3. **Republishing the article for any personal purposes of the authors after taking journal permission.**

To be signed by all authors:

Signature:……..date: ……..

Printed name: ……

Signature:……..date: ……..

Printed name: ……..

Signature:……..date: ……..

Printed name: ……..

Correspondence address:

……
……
……
Address:……
……
……
Telephone:……..email: ……..

Note: Please complete and sign this form and mail it to the below address with your manuscript

The Iraqi Journal of Applied Physics,
P. O. Box 55259, Baghdad 12001, IRAQ
Email: irq_appl_phys@yahoo.com OR editor_ijap@yahoo.co.uk, Mobile: +964-7901274190

IRAQI JOURNAL OF APPLIED PHYSICS

CONTENTS